nuclear fusion
IAEA

PAPER • OPEN ACCESS

SOLPS-ITER modelling of helium transport, recycling and pumping at the ASDEX Upgrade tokamak

To cite this article: A. Zito *et al* 2025 *Nucl. Fusion* **65** 046022

OPEN ACCESS
IOP Publishing | International Atomic Energy Agency
Nuclear Fusion
Nucl. Fusion **65** (2025) 046022 (26pp)
https://doi.org/10.1088/1741-4326/adbe90

SOLPS-ITER modelling of helium transport, recycling and pumping at the ASDEX Upgrade tokamak

A. Zito[1,*], O. Pan[1], M. Wischmeier[1], A. Kappatou[1], A. Kallenbach[1], S.O. Makarov[1,2], M. Bernert[1], M. Cavedon[3], D. Reiter[4], U. Stroth[1,5] and the ASDEX Upgrade Team[a]

[1] Max Planck Institute for Plasma Physics, Boltzmannstr. 2, Garching, Germany
[2] Max Planck Institute for Plasma Physics, Weldensteinstr. 1, Greifswald, Germany
[3] Dipartimento di Fisica G. Occhialini, Universitá di Milano-Bicocca, Milano, Italy
[4] Institute for Laser and Plasma Physics, Heinrich-Heine-University, Düsseldorf, Germany
[5] Physik-Department E28, Technische Universität München, Garching, Germany

E-mail: antonello.zito@ipp.mpg.de

Received 8 December 2024, revised 19 February 2025
Accepted for publication 10 March 2025
Published 24 March 2025

Abstract

Extrapolating the observed behavior of helium exhaust in current tokamaks towards future reactors requires the understanding of the underlying physical mechanisms determining helium transport, recycling and pumping. Helium compression is the main physics-based figure of merit characterizing how efficiently helium is transported towards the divertor and recycled at the target plates. Moreover, helium gas transport in the subdivertor region towards the pumps is strongly influenced by vessel geometry and installed pumps. The SOLPS-ITER code package is used to model H-mode He-seeded deuterium plasmas at the ASDEX Upgrade tokamak, and compared to recent experiments. The simulations generally indicate a poor recycling of helium in the divertor, compared to that of deuterium, in qualitative agreement with the experiment. This is mainly determined by a deeper edge transport barrier and a weaker parallel SOL transport of He ions, with respect to D ions, and by the higher first ionization energy of He atoms, which results in a deeper penetration of recycled atoms into the plasma. The simulated He compression is, however, much smaller than the experimentally measured one, despite the introduction of additional, non-default physics components into the code. Helium gas transport in the subdivertor region towards the pumps is conductance-limited, but moderately enhanced by the entrainment of He atoms into the stronger, viscous deuterium gas flow via friction. The observed poor helium recycling poses challenges in view of the requirements of helium exhaust in future reactors. Our results emphasize the need to investigate further strategies to optimize helium pumping, to guarantee an efficient removal of helium ash in future burning plasmas.

[a] See Zohm *et al* 2024 (https://doi.org/10.1088/1741-4326/ad249d) for the ASDEX Upgrade Team.
[*] Author to whom any correspondence should be addressed.

Additionally, the observed difficulty of SOLPS-ITER in reproducing the experimental observations suggests a careful evaluation of the currently available extrapolations of impurity transport towards future devices obtained via edge transport modelling.

Keywords: helium exhaust, helium compression, SOLPS-ITER, ASDEX Upgrade

(Some figures may appear in colour only in the online journal)

1. Introduction

In future fusion reactors it will be mandatory to keep the concentration of helium 'ash' within tolerable values, in order to avoid fuel dilution and achieve stationary burning [1–3]. The core source of He ions in burning plasmas will be defined by the desired value of fusion power generation [4]. In steady state, this must equate the pumped flux. The He concentrations in different tokamak regions resulting from this balance will depend on a number of interconnected processes, shown in figure 1 and described below, related to both transport physics and technical characteristic of the device. These mostly belong to the tokamak edge region, as core transport has been seen to influence the efficiency of helium exhaust at a much lesser extent [5].

- *Transport in the plasma edge and boundary*. Radial edge transport determines the flux through the separatrix, i.e. leaving the confined plasma [6]. This is closely related to the employed confinement regime and the presence of an edge transport barrier (ETB) [7, 8]. Once in the scrape-off layer (SOL), the parallel transport towards the divertor targets is mostly collisional [9, 10].
- *Recycling at the divertor targets*. Recycled atoms can be transported towards the pumps, or leak towards the main chamber as ions, depending on parallel ion flow in the SOL and ionization mean free path of recycled atoms [11, 12]. Therefore, this is closely related to the divertor operating regime and to the targets geometry [13].
- *Pumping from the subdivertor region*. Neutral gas dynamics determines the neutral density in front of the pumps. This is influenced by subdivertor geometry and viscosity/friction properties of the gas [14]. The employment of active pumps finally determines the pumped flux from this region.

The most convenient way to quantify this is through the following dimensionless parameters:

- A *divertor compression*, defined as

$$C_{\mathrm{He}} \equiv \frac{n_{\mathrm{He}^0}^{\mathrm{div,rec}}}{n_{\mathrm{He}^{2+}}^{\mathrm{plasma}}}, \tag{1}$$

  i.e. as the ratio between neutral He density in the subdivertor recycling volume and He ion density in the edge at the plasma midplane. This parameter describes the interplay between transport and recycling, and will be therefore mostly a device-independent parameter, suitable for direct extrapolations.
- A *subdivertor density ratio*, defined as

$$R_{\mathrm{He}} \equiv \frac{n_{\mathrm{He}^0}^{\mathrm{div,rec}}}{n_{\mathrm{He}^0}^{\mathrm{div,pump}}}, \tag{2}$$

  i.e. as the ratio between subdivertor neutral He densities in the recycling and pumping volumes. This parameter is strongly influenced by the subdivertor geometry and the applied pumping speed, therefore is greatly device-dependent.

A comprehensive knowledge of the physics of helium transport, recycling and pumping is necessary to perform reasonable extrapolations of current experiments towards future reactors. Additionally, it supports the choice of their divertor geometry and the design of their pumping systems. Helium exhaust experiments have been performed in several divertor tokamaks, including JET [15–17], ASDEX Upgrade (AUG) [18–20], JT-60U [21, 22] and DIII-D [23, 24]. The SOLPS-ITER transport code package [25, 26], as well as previous SOLPS versions, have been used to predict helium exhaust in future tokamaks, e.g. while designing the ITER divertor [27–29]. However, edge transport simulations have never been contrasted against experimental helium measurements, to assess their prediction capability, to the best of the authors' knowledge.

We provide here an in-depth comparison between SOLPS-ITER simulations and fully experimental He measurements. For this, we studied recent experiments carried out at the AUG tokamak, already reported in [30]. Whereas [30] was focused on the interpretation of the experimental exhaust dynamics, letting aside SOLPS-ITER predictions, here we focus on the interpretation of the processes defining the steady-state helium transport and recycling. SOLPS-ITER is able to capture virtually all processes directly related to transport and recycling. In spite of this, our results suggest that important pieces of physics potentially affecting the overall helium exhaust are still missing, as will be explained in the text.

In section 2 the performed experiment is briefly summarized. Section 3 provides information about the modelling setup. In section 4 the results used to characterize and interpret helium transport and recycling in the plasma are presented. Section 5 focuses instead on the results used to characterize and interpret helium transport and pumping in the subdivertor

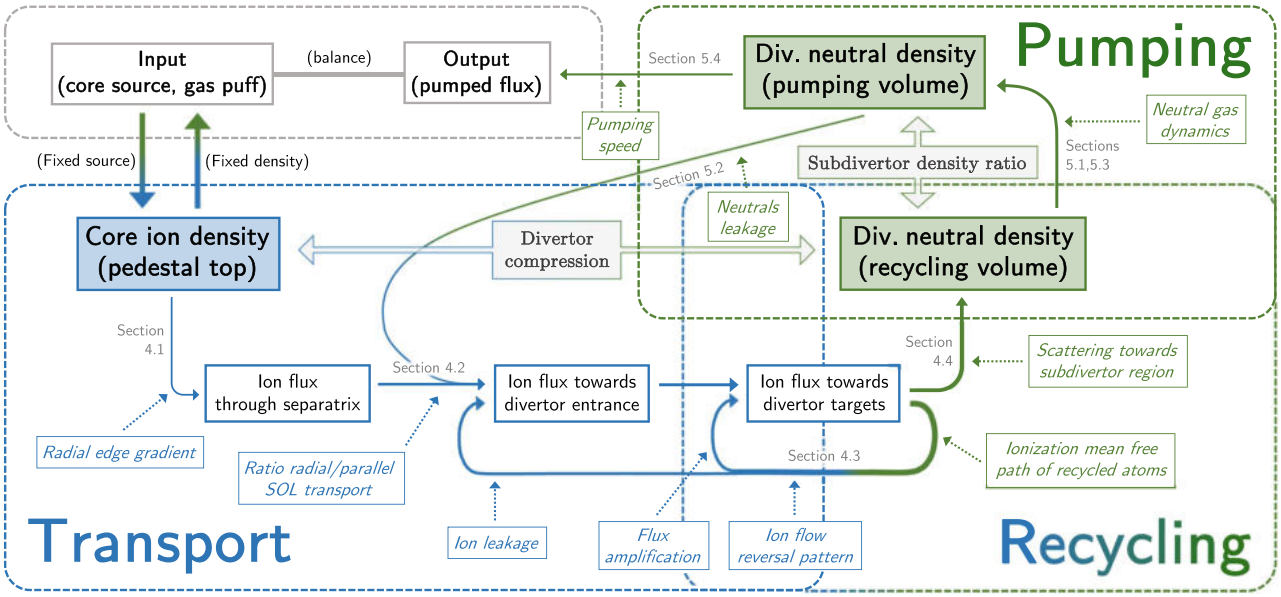

Figure 1. Overview of processes and mechanisms determining helium exhaust in different regions in the edge of a tokamak, and sections of the text in which they are investigated. The input-output balance determines the He densities in the three relevant observable regions (core-edge interface, and the subdivertor recycling and pumping volumes). Blue colors describe ion regions/fluxes, while green colors describe neutrals regions/fluxes.

neutral gas. Sections 6 and 7 provide, respectively, a final discussion and a summary.

2. Experimental setup

Figure 2 shows a poloidal cross section of the device and highlights puffing and pumping locations, regions definitions and employed diagnostics.

2.1. AUG pumping systems

AUG is equipped with a set of 11 toroidally distributed turbomolecular pumps. These provide a total pumping speed of about 7 $m^{-3}\,s^{-1}$ for D_2 molecules [31]. The effective value for He atoms is the same, because it only depends on the mass of the pumped particles. It also features a toroidally symmetric cryopump [32]. This provides a pumping speed of about 120 $m^{-3}\,s^{-1}$ for D_2 molecules [31]. However, it is not effective in capturing He atoms. Its cryopanel surface is indeed kept cooled down by liquid helium, therefore its temperature is not sufficiently low to allow He atoms to condense on it.

2.2. Available diagnostics for He measurements

The He^{2+} ion density profiles at the plasma midplane are measured through a charge-exchange recombination spectroscopy (CXRS) system, based on the ADAS effective CX emission rates [33, 34]. In the evaluation of the absolute He density the plume effect is taken into account [35]. The LOS of the employed core and edge systems are shown in blue and orange, respectively, in figure 2.

Line-integrated radiative emission measurements in the divertor plasma regions are performed observing the emitted light, within the visible range, with CCD cameras. Both HeI and HeII measurements were available in the performed experiments. Some of the LOS covered by this system are shown in red, numbered from 1 to 4, in figure 2.

Neutral He density measurements in the subdivertor region are made with a newly developed type of in-situ optical Penning gauge [36]. This is installed in the region that we defined as the 'pumping volume' (see figure 2). Another gauge is installed in the 'recycling volume', but was not functional at the time of the performed experiments. The He partial pressure, which is directly measured by the gauge, is converted to density assuming the He gas to be at room temperature of 300 K.

2.3. Experimental scenario

We studied the AUG discharge #39149, which is a lower single-null type-I ELMy H-mode, with $B_t = -2.5$ T and $I_p = 0.8$ MA (i.e. with normal field direction, so with $\boldsymbol{B} \times \nabla \boldsymbol{B}$ vector directed towards the X-point at the bottom), with roughly constant D fueling at $1.2 \cdot 10^{22}$ e s^{-1} and moderate N seeding at $2 \cdot 10^{21}$ e s^{-1}, resulting in a high-recycling, moderately attached divertor. Figure 3 shows the He density time traces. The He concentration varies with time, as a 300 ms long He gas puff at $2.5 \cdot 10^{21}$ e s^{-1} is performed from a midplane fueling valve.

The time-dependent behavior of the He concentration in this discharge was already interpreted with the numerical model described in [30]. The He density time traces in figure 3 show that the time-dependent behavior of helium is the same

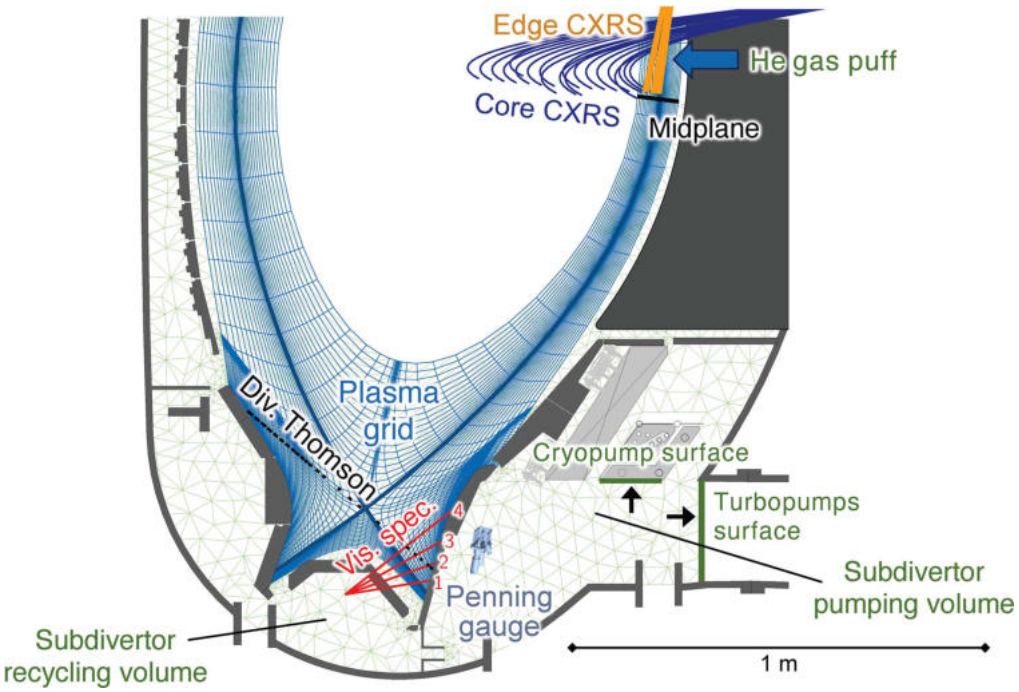

Figure 2. Poloidal view of the lower section of AUG. Employed diagnostics, puffing locations, pumping systems and region definitions as used in the text are highlighted. The B2.5 grid is shown in blue, while the Eirene grid is shown in green.

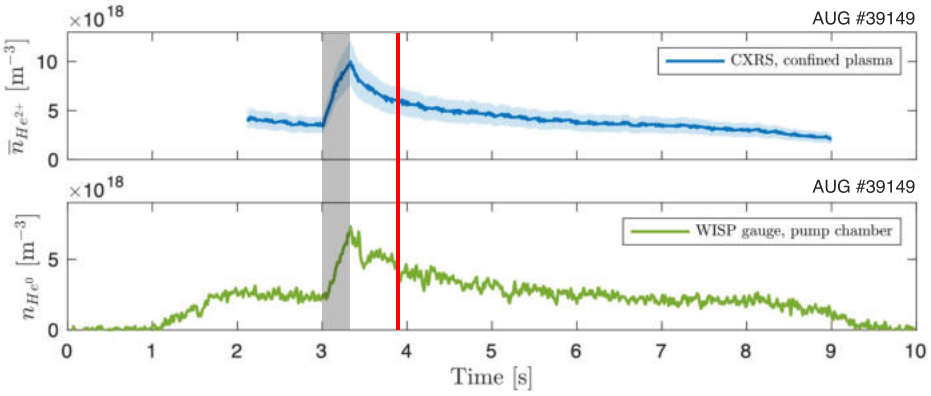

Figure 3. He density time traces from the analyzed AUG discharge #39149. From top to bottom: average core He^{2+} ion density from CXRS (obtained by radially integrating the measured core profile) and neutral He atom density in the pumping volume from the optical Penning gauge. Error bars of CXRS data are given as shaded areas. For other time traces for the same discharge we refer to [30].

in the various regions of the plasma and the exhaust gas. When normalized, the signals from CXRS and Penning gauge overlap, and no temporal delay is visible. Therefore, neither the relative He concentration nor the intensity of wall fueling/pumping, which do change during the discharge, affect divertor compression and subdivertor density ratio. These are constant, and only depend on the plasma background. In other words, the processes defining helium transport, recycling and pumping are unrelated to (and independent from) the exhaust dynamics. This allows to study the former aspects with a steady-state SOLPS-ITER simulation. For this, we selected the time $t = 3.9$ s, indicated with a red vertical line in figure 3.

Since neutral He density measurements were not available for the subdivertor recycling volume, an assumption for this was necessary. For the D_2 gas, the subdivertor density ratio lies within the range $4-5$, as measured by ionization gauges [37, 38] operating in both volumes. This is caused by the flow resistance caused by the subdivertor geometry and by the intensity of the pumping sink. The geometry effect is the same for D_2 molecules and He atoms, since they have the same mass. However, the pumping sink is much less intense for the He atoms. It is experimentally shown that this ratio, for D_2 molecules, drops from $4-5$ to roughly $1.5-2$ if the cryopump is switched off. We assume therefore that the behavior of a pure D_2 gas in a situation without cryopump would emulate

that of a He gas, and hence that the subdivertor density ratio for He atoms is also roughly 1.75. As section 5.1 will explain, the modelling results support, *a posteriori*, this assumption.

3. Modelling setup

SOLPS-ITER consists of the self-consistent coupling of two distinct physics modules, namely the multi-species fluid plasma transport code B2.5 and the kinetic neutral transport code Eirene. The first one solves the fluid equations for density, parallel momentum, electron/ion thermal energy and current [39]. The second one solves the kinetic Boltzmann equation for atoms and molecules, simulating the trajectories of neutral test particles with Monte Carlo methods [40].

The goal of the modelling activity was the best possible simulation of the AUG discharge #39149. For this we performed coupled B2.5-Eirene runs featuring D, N and He as plasma species.

3.1. Computational grid

Figure 2 shows the employed computational grid. The field-aligned B2.5 grid in which the plasma transport equations are solved is based upon the experimental magnetic equilibrium.

The gas puff source for D_2 molecules and N atoms is set in the divertor plasma region, while for He atoms it is set at the outer midplane. Two pumping surfaces, simulating the effect of the cryopump and the turbomolecular pumps, were defined in terms of capture coefficients C_{capture} (i.e. the probability that an incident particle is absorbed). For the D_2 gas we set the values to 0.20 and 0.007 for the cryo- and the turbopumps, respectively. Within Eirene, this can be related to the effective pumping speed S_{gas} for a gas species with temperature T_{gas} (in K) and mass m_{gas} (in AMU) through the formula [41]

$$S = 36.38 \cdot A \cdot C_{\text{capture}} \cdot \sqrt{T_{\text{gas}}/m_{\text{gas}}}, \tag{3}$$

where A is the pumping surface area. Given the two pumping areas as defined in the Eirene grid (cf figure 2), these values simulate the measured pumping speeds $S_{\text{cryo}} = 120\ \text{m}^{-3}\,\text{s}^{-1}$ and $S_{\text{turbo}} = 7\ \text{m}^{-3}\,\text{s}^{-1}$ (cf section 2.1), assuming a gas temperature of 300 K. Regarding the He gas, for the cryopump we set a capture coefficient of 0, while the value for the turbopumps is the same as the one employed for the D_2 gas.

All material surfaces are tungsten, as in the experiment. Accordingly, coefficients extracted from a TRIM-generated database (reflection probabilities, angles and energies) are employed to simulate the reflection of ions as fast neutrals at the surface boundaries [42]. The surface temperatures determine the energy at which the non-reflected ions are re-emitted as thermal neutrals. We used 0.1 eV ($\approx$ 1160 K) for the targets, 0.001 eV ($\approx$ 11.6 K) for the cryopump surface, and 0.025 eV ($\approx$300 K, i.e. room temperature) for all other surfaces.

3.2. Atomic, molecular and neutrals reactions

Cross sections and rate coefficients for the atomic and molecular processes simulated by Eirene are extracted from the AMJUEL and HYDHEL databases [43]. For D atoms and D_2 molecules the standard set of reactions was used (see e.g. [44]). This includes electron-impact dissociation and ionization, radiative and dissociative recombination, CX collisions and elastic scattering. For impurities, only electron-impact ionization and recombination are included by default. For He atoms, in the course of our investigation we also included several reactions not included by default in the Eirene reaction dataset, namely CX collisions with He ions and D ions, and elastic collisions with D ions [45]. The impact of such additional reactions is expected to be relevant when temperatures drop down to the order of few eV. Figure 4 shows the rate coefficients of the reactions involving He atoms, and the resulting mean free paths.

Neutral-neutral collisions can be modelled running Eirene in non-linear mode employing a BGK approximation for the treatment of the collision integral in the Boltzmann equation [46, 47]. These are usually not activated to save computational time, apart from when dealing with larger devices [48]. They would allow to model neutral gas viscosity and inter-species friction. Although impurity gas flows are unlikely to exhibit any self-resistance due their own viscosity, because of their low partial pressure, a drag effect due to inter-species friction may not be ruled out. In order to investigate this, we included in our simulations self-collisions for D atoms, D_2 molecules and He atoms, and cross-collisions between these species. Figure 5 shows the collision frequencies for self- and cross-collisions for D_2 and He, calculated employing a rigid-sphere model for the gas particles, and the resulting BGK mean free paths. Unless otherwise specified, all simulations are performed with neutral-neutral collisions activated.

3.3. Physics input parameters

The main physics-based input parameters for the simulations are particle sources, heating power and anomalous transport coefficients describing radial transport.

For D we imposed a constant D^+ ion density of $3.5 \cdot 10^{19}$ m^{-3} at the core boundary as fixed boundary condition. For N atoms, which only serve as a radiating impurity in our scenario, we imposed an arbitrary fueling rate in such a way to roughly reproduce the experimentally measured radiation in the SOL and divertor regions. Finally, we imposed a constant He^{2+} ion density of $5 \cdot 10^{18}$ m^{-3} at the core boundary as fixed boundary condition, to reproduce the radially outermost core CXRS measurement (cf figure 8(*a*)).

We imposed an input power by specifying the electron and ion energy fluxes crossing the core plasma boundary (which is around $\rho_p = 0.9$ for the employed grid). A total input power of 5 MW is used. We calculated this from the difference between the total input power and the experimentally measured radiated power in the region at $\rho_p < 0.9$ applying a tomographic analysis on the bolometric measurements [49]. This is shared as 3 MW for the electron channel and 2 MW for the ion channel.

Regarding the transport coefficients, we empirically defined radial profiles for particle diffusivity D_n and electron and ion thermal diffusivities χ_e, χ_i, driving the anomalous

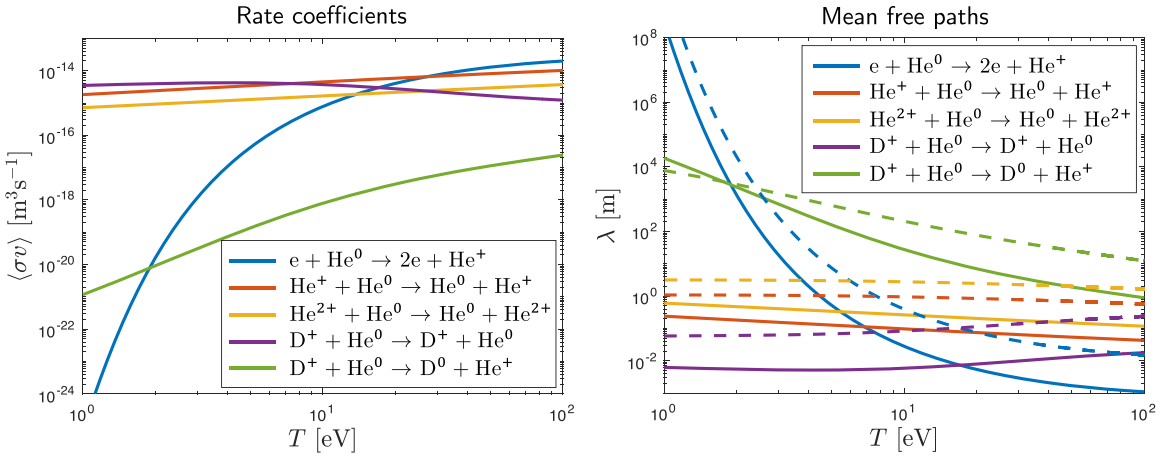

Figure 4. Left: rate coefficients for electron-impact He ionization, He–He CX collisions, D-He elastic collision and D-He CX collision, as functions of the temperature of the electrons or of the involved ion. An electron density of 10^{20} m^{-3} is assumed. Right: resulting mean free paths, estimated as $\lambda = \frac{\bar{v}_{He^0}}{n\langle\sigma v\rangle}$, where $\bar{v}_{He^0} = \sqrt{E_{He}/m_{He}}$, and n is the density of the electrons or of the involved ion. These are estimated assuming $n_{He^{+/2+}} = 0.05\,n_e$ and $n_{D^+} = n_e$. Solid lines represent a case with $E_{He^0} = 0.1$ eV (which is characteristic of the thermally re-emitted atoms), while dashed lines represent a case with $E_{He^0} = 20$ eV (which is characteristic of the fast reflected atoms).

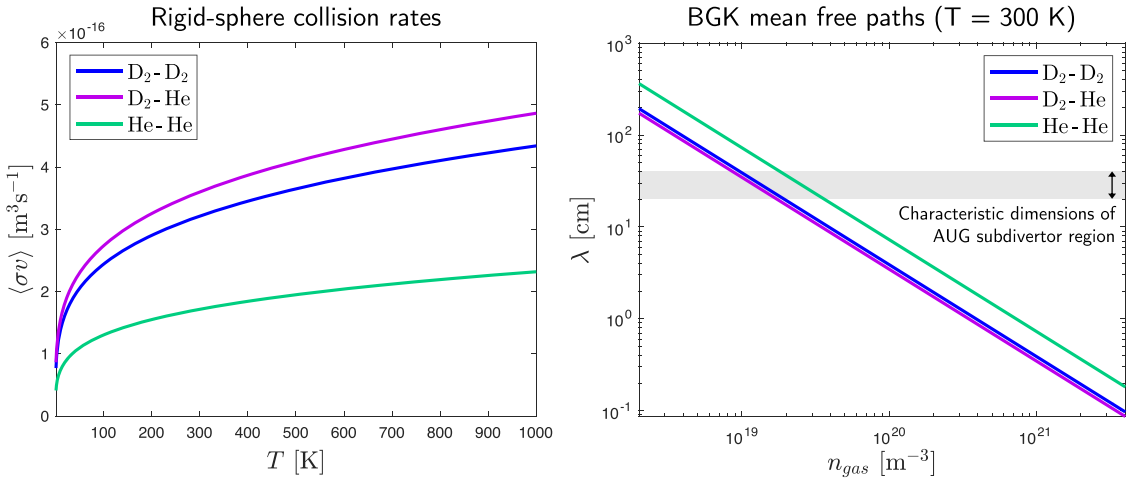

Figure 5. Left: Rate coefficients for self- and cross-collisions between D_2 molecules and He atoms, calculated using a rigid sphere model, as function of the gas temperature. Right: resulting mean free paths, as function of the gas density, estimated employing a BGK approximation, at room temperature. For the D_2-He collision, He is considered as a projectile in a D_2 background gas, so n_{gas} in this case corresponds to the D_2 density.

radial fluxes. Radial particle transport is treated as purely diffusive for all species. In this sense, D_n must be considered as an 'effective' particle diffusivity [50].

3.4. Background plasma solution

Figure 6 shows several simulated radial plasma profiles at the outer midplane and in the divertor volume, as well as the corresponding experimental measurements.

The match between simulated and experimental profiles at the outer midplane was achieved after a fine tuning of the anomalous transport coefficients profiles. For the particle diffusivity of the main ion species we employed the optimization algorithm described in [51]. The electron density (figure 6(*a*)) is compared to the result of a bayesian integrated data analysis [52], obtained combining measurements of different diagnostics, including lithium-beam emission spectroscopy [53, 54] and core/edge Thomson scattering (TS) [55, 56]. The electron temperature (figure 6(*b*)) is also compared with core/edge TS measurements. The ion temperature (figure 6(*c*)) is compared with core/edge CXRS measurements [57, 58]. The ETB needed to reproduce the pedestal for all profiles is clearly visible. Following the evidence of enhanced divertor transport [59], all such coefficients were multiplied by 3 in the divertor region [6] with respect to the values imposed at the outer midplane.

[6] With divertor region we define the region belonging to the computational grid whose cell poloidally lie further from the X-point cut, but not in the PFR.

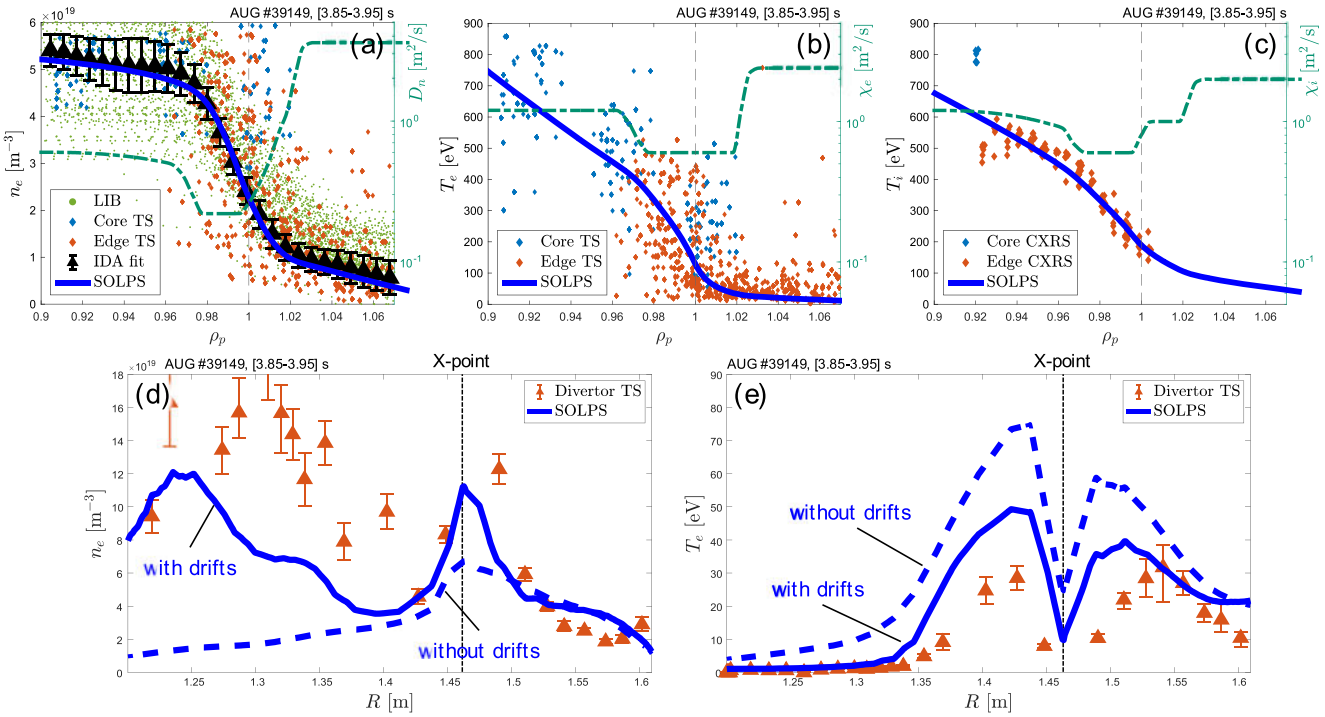

Figure 6. Comparison between simulated plasma profiles in several regions of the plasma, as blue lines, and experimental data from different diagnostics as colored points. Top row: electron density (*a*), electron temperature (*b*) and ion temperature (*c*) at the outer midplane (see figure 2 for the midplane definition). The relative anomalous transport coefficients profiles (with particle diffusivity referred to the main ion species for (*a*)) are shown as dashed green lines. Bottom row: electron density (*d*) and electron temperature (*e*) in the divertor volume along the divertor TS laser path (shown in black in figure 2), for both cases without and with drifts activated.

We performed simulations both without and with drifts flows, which strongly enhance the asymmetries between inner and outer divertor [60–62]. The bottom row of figure 6 shows the simulated electron density and temperature profiles within the divertor plasma volume, compared with divertor TS measurements [63]. Boundary conditions and anomalous transport coefficients were adapted in order to achieve the same midplane profiles both without and with drifts. The case with drifts activated shows a much better, albeit still not perfect, agreement with the experimental measurements, including e.g. a lower electron temperature and the formation of an high field side high density region [64].

4. Characterization of helium ion transport and recycling

This section discusses the first set of processes described in figure 1, i.e. related to the transport of He ions in the plasma and their recycling in the divertor.

The main figure of merit in this regard is the divertor compression C_{He} (equation (1)) for helium. It is worthwhile to note that, as helium is not a radiating impurity, its presence is not expected to significantly alter the background plasma solution, even if in non-trace amounts, like in the investigated scenario. While ramping the He concentration at the plasma midplane, in our simulations, up to the experimental value, we observed indeed that simulated state variables, main ion and energy fluxes and global power balance do not change. Therefore, the properties of helium transport and recycling do not depend on the He concentration itself. This is consistent with the experimental observation of He compression being independent on the He concentration in a constant background plasma (cf figure 3). This behavior differs from that of radiating impurities, which is also determined by the change in the plasma background due to radiative losses [65–68].

The SOLPS-ITER grid does not extend further internally in the core than $\rho_p = 0.9$. Therefore, for the definition of the divertor compression (equation (1)) we employ the value of the He^{2+} density at the core boundary of the grid as denominator. Consistently, the core CXRS measurement at the same radial location is also used for its experimental counterpart. For both experiment and simulation (for the latter as boundary condition), this value is $5.0 \cdot 10^{18}$ m^{-3} (cf figure 8(*a*)). At the same time, the experimentally measured He atom density in the subdivertor pumping volume from the optical Penning gauge is $4.5 \cdot 10^{18}$ m^{-3} (see figure 3). Assuming a subdivertor density ratio of 1.75 (cf section 2.3), hence a value of $7.9 \cdot 10^{18}$ m^{-3} for the He atom density in the subdivertor recycling volume, this results in an experimental He compression of 1.6 [30].

We consider, in first instance, a simulation performed using the default physics model included in SOLPS-ITER. The default model consists of the B2SOLPS5.2 version of the plasma solver [69], no drifts terms for the plasma fluid equations and atomic physics model for neutral impurities which only includes ionization and recombination reactions.

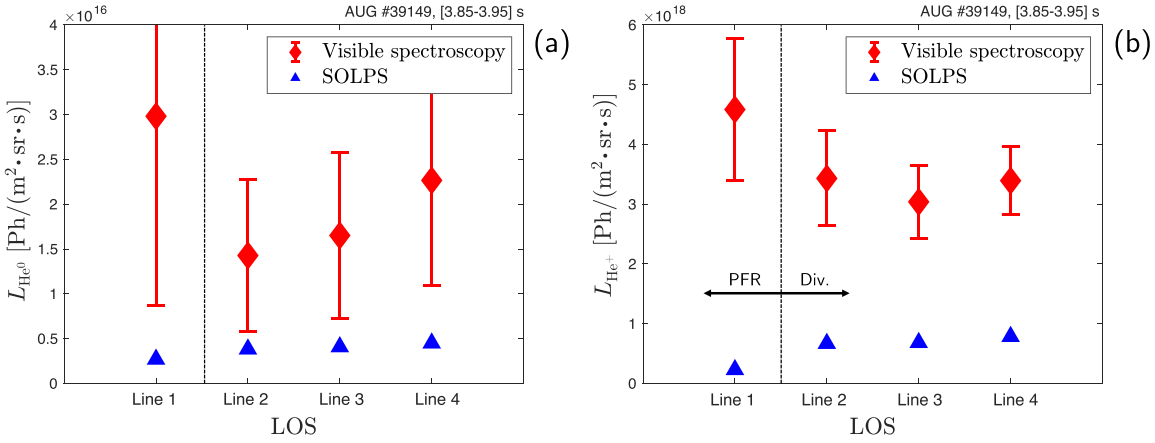

Figure 7. Comparison between experimental line-integrated emission in the divertor plasma volume, in red, and simulated ones, in blue. The lines of sight correspond to the red lines in figure 2. The synthetic emissivities ε are calculated from the plasma solution using the simulated electron and He atom/ion densities, and the photo-emission coefficients (PECs) extracted from the ADAS ADF15 database [34], as $\varepsilon_z(n_e,T_e) = n_e \cdot n_z \cdot \mathrm{PEC}_{\mathrm{exc}}(n_e,T_e) + n_e \cdot n_{z+1} \cdot \mathrm{PEC}_{\mathrm{rec}}(n_e,T_e)$. The synthetic line-integrated emissions are finally calculated as $L = \frac{1}{4\pi}\int_{\mathrm{LOS}} \varepsilon \, \mathrm{d}s$. Left: HeI line emission corresponding to the 1s4p $\rightarrow$ 1s2s transition at 396.5 nm. Right: HeII line emission corresponding to the $n = 4 \rightarrow n = 3$ transition at 468.6 nm. Other collisional radiative models which might be used to evaluate the synthetic line emissions from the plasma solutions, such as the Goto model [71], are expected to yield similar results [72].

Table 1. Simulated values of total ion densities and total ion fluxes in characteristic regions of the computational domain, for deuterium and helium. Densities are in m^{-3}, fluxes are in s^{-1}.

	Core ion density(pedestal top)	Ion flux through sep.	Ion flux towards divertor entrance	Ion flux towards divertor targets	Subdiv. neutr. density (recycling volume)	Divertor compression
D	$3.50{\cdot}10^{19}$ (B.C.)	$8.97{\cdot}10^{21}$	$1.55{\cdot}10^{22}$	$1.02{\cdot}10^{23}$	$6.62{\cdot}10^{19}$ (molecules)	**3.78**
He	$5.00{\cdot}10^{18}$ (B.C.)	$6.94{\cdot}10^{20}$	$4.86{\cdot}10^{20}$	$1.09{\cdot}10^{21}$	$5.78{\cdot}10^{17}$ (atoms)	**0.12**
Ratio	**0.143**	0.077	0.031	0.011	**0.004** $\left(\frac{\mathrm{He}}{2\cdot\mathrm{D}}\right)$	

The impact of enhancing the complexity of such model will be addressed in the section 4.6.

The simulated He atom density in the subdivertor recycling volume is only $5.78 \cdot 10^{17}$ m^{-3} (cf figure 15(*b*)). Therefore, the simulated He compression is 0.12. At the same time, the simulated value for D is 3.78 [7]. Therefore, the simulated He concentration (with respect to the main species) decreases from 14.3% at the pedestal top to 0.4% in the subdivertor gas. This shows a strong de-enrichment of helium, which is qualitatively in line with the experimentally observed trend [70]. However, it also shows a serious underestimation of the experimental measurement, by a factor of more than 10. This is also visible in the line-integrated emission from the divertor plasma volume (figure 7), where the simulated values are lower than the experimental ones by a roughly similar factor. Figure 7 should be interpreted with caution, as the simulated line-integrated emission also depends on the background electron density and temperature, which are not perfectly matched in the divertor (cf figures 6(*d*) and (*e*)). However, since the mismatch between experiment and simulation is similar for divertor line emission and subdivertor partial pressure, we assume that the mismatch for the divertor line emission is also caused by a simulated He density in the divertor being smaller than in experiment. The divertor de-enrichment of helium with respect to the main species is interpreted analyzing the simulated fluxes on the way between pedestal top (whose density is the denominator of equation (1)) and subdivertor recycling volume (whose density is the numerator of equation (1)), according to figure 1. These are listed in table 1.

Divertor compression can be therefore interpreted as the result of a series of processes, taking place in different regions of the plasma. These determine how the particle fluxes leaving the core evolve while travelling towards the divertor (i.e. reading table 1 from the left to the right). Comparing the relative evolution between D and He (bottom line), it can be seen that, going from left to right, their ratio constantly decreases. In order words, while travelling from the core to the divertor, the He particle flow gradually weakens, in relative intensity, with respect to the D particle flow. This results in a much lower divertor neutral He concentration relative to the core He concentration. In the following subsections, the reason for this will be analyzed, focusing on one region at a time.

4.1. Influence of edge transport

The transport processes taking place in the plasma edge determine the ion fluxes crossing the separatrix and leaving the confined region, for a given ion density at the pedestal top

[7] For calculating this quantity, twice the deuterium neutral density in the subdivertor region is used, which exists mostly in form of molecules, to account for the presence of two D atoms within a single molecule.

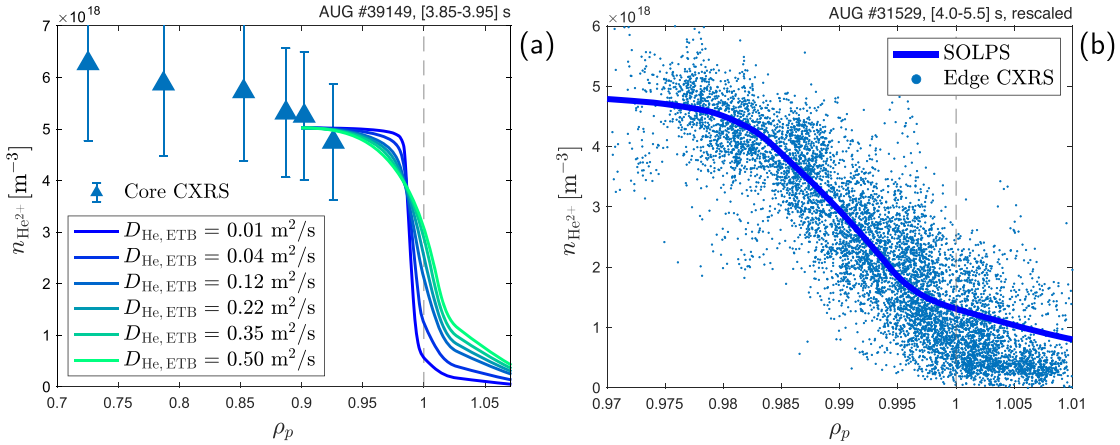

Figure 8. (*a*) Various possibilities for the simulated radial He^{2+} ion density profile at the outer midplane, constrained by the same core boundary condition compatible with the experimental core CXRS measurements, as function of the ETB depth. (*b*) Zoom-in on the simulated profile achieved using $D_{\mathrm{He,ETB}} = 0.04$ m^{-2} s^{-1}, corresponding to the simulations used for the rest of the analysis, compared to the (rescaled) edge CXRS measurements from a similar AUG discharge, documented in [73].

(which is an experiment-based boundary condition in our simulations). In type-I ELMy H-modes an ETB is formed here, in which turbulence is substantially suppressed and inter-ELM radial transport of impurity ions is dominated by neoclassical mechanisms [8].

For the main species, we set a value of the particle diffusivity D_n in the ETB of 0.22 m^{-2} s^{-1}. This is empirically chosen to reproduce the experimentally observed pedestal steepness of the electron density (cf figure 6(*a*)). For the analyzed discharge no edge CXRS data were available for comparison with the modelling. The knowledge of the pedestal steepness for the He^{2+} ion density is, however, critical. Performing several simulations with different, yet reasonable, values of the particle diffusivity for He within the ETB with the same pedestal top density (figure 8(*a*)) reveals a strong change of the ion flux through the separatrix. This, in turn, also causes a difference in the simulated He compression up to a factor of 5. Therefore, setting an appropriate value of D_n for helium in ETB is of great importance for the simulation fidelity.

In spite of the fact that no edge CXRS data were available for the AUG discharge #39149, we could rely on past measurements from another type-I ELMy H-mode at AUG, sufficiently similar to the investigated one, reported in [73], in which inter-ELM edge CXRS measurements for the He^{2+} ion density were available. These are shown in figure 8(*b*). Noticeably, the pedestal of the He^{2+} ion density is steeper than the electron density one. Such gradient could be reproduced imposing, for both He^{+} and He^{2+} ion species, a value of the particle diffusivity D_n in the ETB of 0.04 m^{-2} s^{-1}, i.e. much lower than the one imposed for the main ion species. We stress that, in the performed modelling, the employed 'effective' diffusivity accounts for the combined effects of diffusive and convective transport, since we do not define an inward pinch velocity.

This shows that the de-enrichment of the He ion flux through the separatrix, with respect to that of the main species, from 14.3% to 7.7% (cf table 1), is caused by the different neoclassical transport within the ETB, at least for H-modes. It also suggests that such effect might be even more important for heavier impurities, in view of the dependence of the neoclassical transport level (in particular the inward convection) with the ion charge [8].

4.2. *Influence of SOL transport*

The competition between parallel and radial transport in the SOL determines the ion flux reaching the divertor entrance (which we define as the radial surface, in the computational domain, crossing the X-point), for a given ion flux crossing the separatrix.

For the main ion species, the effective particle diffusivity D_n increases from roughly 0.5 m^{-2} s^{-1} in the near SOL up to roughly $3-4$ m^{-2} s^{-1} in the far SOL, to reproduce the experimental electron density profile (cf figure 6(*a*)). Absolute impurity density measurements outside the separatrix are, however, not possible. As such, no empirical evidence exists about how radial SOL transport of He ions should be accounted. The most reasonable assumption was to impose, for both He^{+} and He^{2+} ion species, the same value of particle diffusivity D_n in the SOL as for the main ion species.

The resulting difference between D and He ions, in terms of SOL transport, can be shown performing a global particle balance for both in the SOL volume. A continuity equation as the one solved by SOLPS-ITER for the ion species α, at steady state, reads[8],

$$\frac{\partial}{\partial x}\Gamma_{x,\alpha} + \frac{\partial}{\partial y}\Gamma_{y,\alpha} = S_{\alpha}^{\mathrm{vol}}. \tag{4}$$

[8] In equation (4) the metric coefficients are left out, for ease of reading. For the complete form of the continuity equation solved by SOLPS-ITER, we refer to [39].

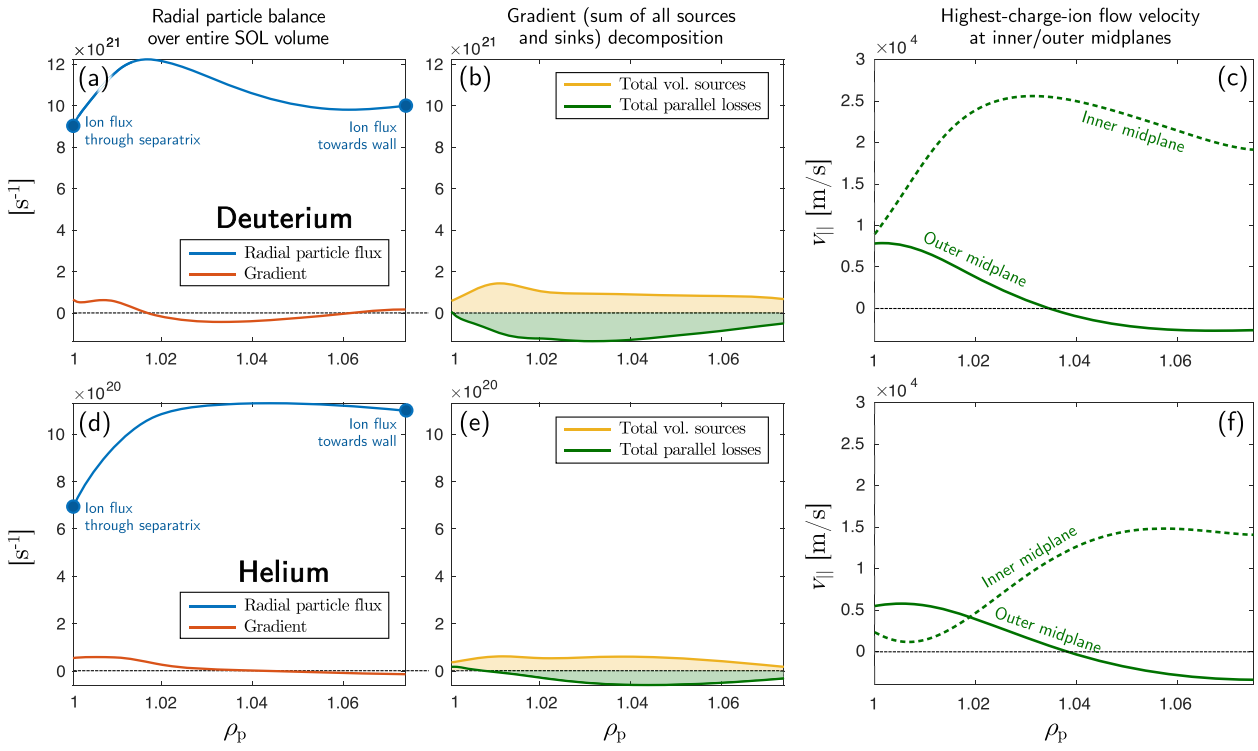

Figure 9. Particle balance in the SOL, applied to the main species (i.e. to the D^+ ions, in the top row) and to helium (i.e. summed over the He^+ and He^{2+} ions, in the bottom row). Plots in the left and middle column: radial particle balance performed in the SOL volume, i.e. poloidally extending from inner to outer divertor entrances and radially up to the main wall boundary. The blue line in (*a*) and (*d*) is the poloidally-integrated radial particle flux. The red line in (*a*) and (*d*) is the radial gradient of the radial particle flux. This can be decomposed into volumetric sources and parallel losses (in yellow and green respectively, in (*b*) and (*e*)). Plots in the right column ((*c*) and (*f*)): radial profiles of the simulated parallel flow velocity for the highest-charge ion, at the inner (dashed lines) and outer (solid lines) SOL midplanes. Here, positive values indicate particles travelling towards the inner divertor.

Here Γ indicate the fluxes, and S^{vol} indicates the volumetric source. x, y indicate the poloidal and radial direction, respectively. Integrating both sides in radial direction, we find

$$\Gamma_{y,\alpha}\left(\rho_p\right) = \int_1^{\rho_p} \left(\frac{\partial}{\partial x} \Gamma_{x,\alpha}\left(\rho_p'\right) + S_\alpha^{\mathrm{vol}}\left(\rho_p'\right) \right) \mathrm{d}\rho_p'. \quad (5)$$

Namely, the variation of the radial particle flux crossing any entire flux surface, with respect to the radial particle flux crossing the separatrix, is balanced by the cumulative parallel particle loss and the cumulative particle source, i.e. occurring between $\rho_p = 1$ and that given flux surface. Figure 9 shows the results of such balance.

For the main species, the particle flux towards the wall is similar to the particle flux crossing the separatrix (blue line in figure 9(*a*)). The cumulative parallel particle loss is indeed roughly balanced by the cumulative volumetric particle source (green and yellow areas, respectively, in figure 9(*b*)). For helium, instead, the particle flux towards the wall is larger than the one crossing the separatrix (blue line in figure 9(*d*)). This is because the cumulative parallel particle loss is smaller than the cumulative volumetric particle source (green and yellow areas, respectively, in figure 9(*e*)). Therefore, He ions are more easily transported to the main wall rather than to the divertor, with respect to D ions. Since the radial transport coefficients in the SOL are the same for both species, this is necessarily linked to the different characteristics of parallel transport between the two species. Figures 9(*c*) and (*f*) show that, especially in the near SOL, where the ion density is higher, the parallel flow velocity of He ions is smaller than that of the main species, consistently with the results of the balance. This can be therefore invoked as the main reason for the further de-enrichment of the He particle flow while travelling from separatrix to divertor entrance, from 7.7% to 3.1% (cf table 1).

4.3. *Influence of divertor recycling*

The interplay between the parallel ion flow and the neutral recycling pattern from the divertor targets determines the ion flux impinging on the divertor targets, for a given ion flux entering the divertor volume [65–68].

In high recycling conditions, neutrals emitted from the divertor targets undergo on average several wall release/re-ionization cycles before being scattered towards the subdivertor volume [74–76]. Given the short time scale of this process, this effectively 'amplifies' the ion flux onto the targets, with respect to a given ion flux entering the divertor region (cf table 1). This process is influenced by the possible existence of a region with ion flow reversal, which is usually the case for

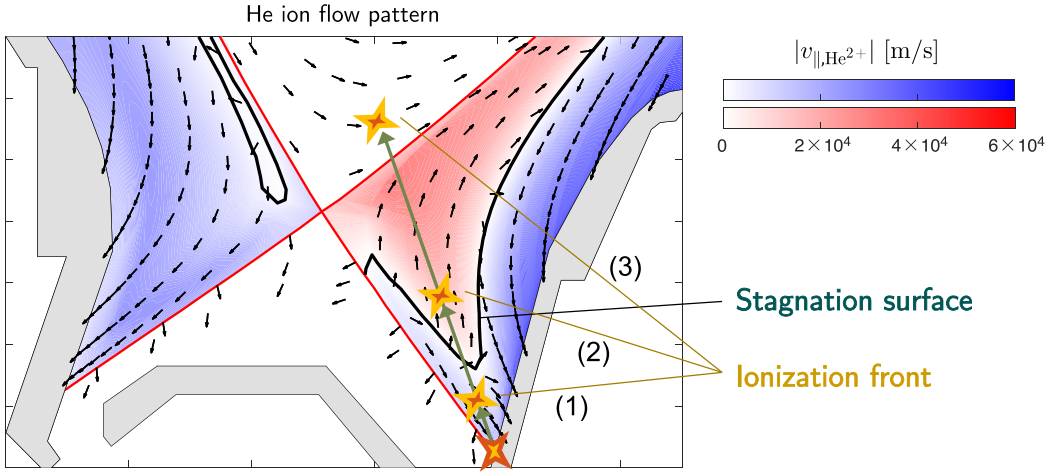

Figure 10. Simulated flow velocity field of the He^{2+} ions. The arrows indicate the direction of the flow. The color intensity (from white to blue/red), only present in the SOL, indicates the absolute value of the flow velocity. Here, blue and red colors indicate regions with forward and reversed flow, respectively (with respect to the closest target).

impurities in high recycling conditions [11, 12]. The boundary between the regions with forward and reversed flow constitutes a 'stagnation surface' for the parallel ion flow. Figure 10 shows the simulated flow velocity field for the He ions in the divertor plasma volume. Especially at the low field side, a large fraction of the divertor volume exhibits, as expected, flow reversal.

The amount of He ion leakage depends on the location where the recycled He atoms are re-ionized, with respect to the position of the stagnation surface of the He ion flow:

- If He atoms are ionized close to the targets, i.e. in the region below the He ion stagnation surface (case (1) in figure 10), they are promptly returned as ions to the targets. This favours the target flux amplification, i.e. maximizes the recycled flux.
- If, instead, recycled He atoms are ionized above the He ion stagnation surface (case (2) in figure 10), they are leaked as ions towards upstream. This increases the return time to the targets, hindering the flux amplification, and reduces therefore the recycled flux.
- An even worse situation arises if the recycled He atoms can penetrate the confined region before being re-ionized (case (3) in figure 10). In this case, the resulting He ions are confined again, drastically reducing the recycled flux.

The interplay between location of the stagnation surface of the He ion flow and ionization front of the recycled He atoms determined therefore the divertor recycling.

4.3.1. Interpretation of the He ion flow pattern in the divertor. The mechanisms determining the two-dimensional flow pattern of the He ions in the divertor volume can be quantified in terms of the various forces acting on the He ions. The interested reader may refer to [77] for a description of the parallel momentum balance equation solved by SOLPS-ITER and to [66] for a description of the parallel force balance determining the ion flow pattern for impurities.

In such a balance, the inertial acceleration and viscous effects are usually negligible, and the most relevant parallel forces applied on He ions are [11, 12]:

- The friction forces, exerted on the He ions due to collisions with all other ion species (but mostly with the main ions), arising because of the difference in their parallel flow velocity. This results in He ions dragged in the same direction of the main ion flow.
- The thermal forces, caused by the parallel temperature variation in the SOL. Less momentum is indeed transferred from other ions arriving from higher temperature region (i.e. from upstream) to He ions, because of the temperature dependence of the collisional momentum transfer. The resulting net force pushes the impurities up the temperature gradient, i.e. towards upstream.

These two terms are therefore in competition, and their balance is greatly sensitive to the divertor plasma conditions (density, temperature and main ion flows). The balance determines the direction of the parallel He ion flow across the divertor plasma, and consequently the position of its stagnation surface, i.e. the black boundary surface in figure 10.

4.3.2. Interpretation of the ionization of recycled He atoms. The ionization mean free path of recycled He atoms determines whether they are ionized below or above the stagnation surface. This mainly depends on the electron temperature in the divertor (cf figure 4).

Figure 11 shows the simulated volumetric ion source from first ionization of neutral atoms in the divertor volume, for D and for He, and relates it to the corresponding ion flow stagnation surface. He atoms penetrate much deeper into the plasma than D atoms. This is consistent with the first ionization energy of He atoms (24.6 eV) being much larger than those of D atoms (13.6 eV). This effect overcomes the lower thermal velocity of He atoms, with respect to D atoms, because of their larger

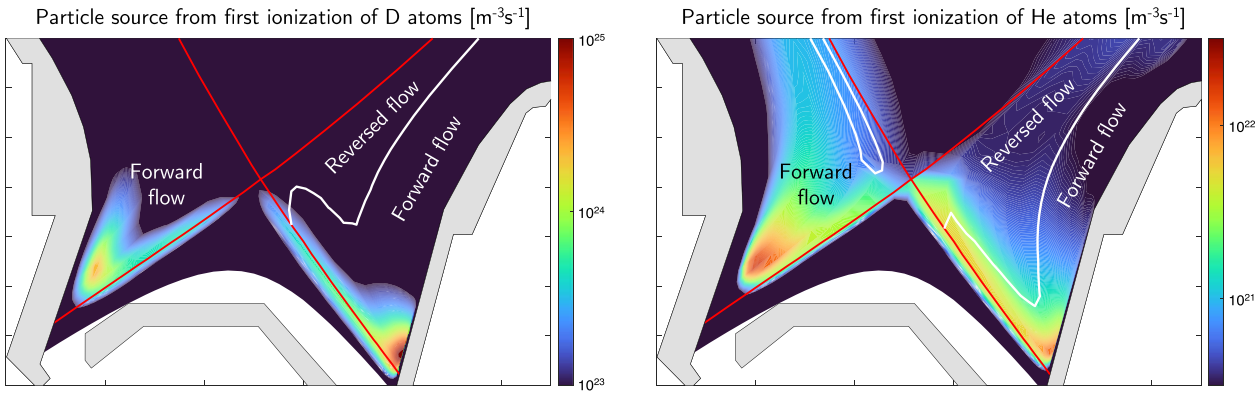

Figure 11. Simulated distributions of the volumetric ion sources from first ionization of D atoms (i.e. the density rate of the reaction $D^0 + e \rightarrow D^+ + 2e$) at the left, and of He atoms (i.e. the density rate of the reaction $He^0 + e \rightarrow He^+ + 2e$), at the right. The stagnation surfaces of the corresponding ion flows are represented as white lines.

Table 2. Calculated fractions of test particles (D and He atoms) followed by Eirene and generated from divertor recycling, ionized in any of the relevant plasma regions (SOL with corresponding ion flow in forward direction, SOL with corresponding ion flow in reversed direction, PFR and core). We show both the calculated fractions from particles recycled from the inner and outer targets separately, and the total one. The latter is not the arithmetic average of the individual contributions, but weighted on the recycled fluxes from both targets.

		SOL (forw.)	SOL (rev.)	PFR	Core
D	*From inner target*	79.8%	1.3%	14.0%	4.9%
	From outer target	73.3%	3.6%	20.2%	2.9%
	Total	**76.1%**	**2.6%**	**17.5%**	**3.8%**
He	*From inner target*	67.6%	12.5%	6.7%	13.2%
	From outer target	44.8%	25.1%	6.5%	23.6%
	Total	**58.4%**	**17.6%**	**6.6%**	**17.4%**

mass. The same repationship between first ionization energy and ionization front has been also observed experimentally for other impurities [78].

The major difference between He and D is not, however, the location of the peak source, which is in both cases rather close to the targets. Rather, the ionization of He atoms is spread quite far from the peak location towards upstream, while that of D atoms is mostly localized close to the peak location. Because of this, a non negligible fraction of the recycled He atoms is recycled above the stagnation surface of the He ion flow, which favours ion leakage. This happens especially at the low field side, where the most extended flow reversal region exists.

4.3.3. Impact on ion leakage from the divertor. The interplay between stagnation surface of the ion flow and ionization front of the recycled atoms can be quantitatively evaluated. For this we followed a sufficiently high number of test particle trajectories simulated by Eirene, from atoms recycled from the divertor targets, and classified them according to whether the first ionization event takes place (i) in a portion of the SOL with forward flow, (ii) in a portion of the SOL with reversed flow, (iii) in the PFR or (iv) in the core.

As discussed, the most favourable situation for flux amplification is the first case, which would ensure a prompt return of the ions to the targets. The second and the fourth case, instead, favour ion leakage. Table 2 shows the results of this calculation, for both D and He.

Only a minority of the recycled D atoms (around 6%) is re-ionized in an unfavourable region. This fraction is much higher for recycled He atoms (i.e. around 35%). This causes a stronger leakage of He ions towards upstream, with respect to D ions. It strongly reduces in turn their flux amplification onto the targets, and is the reason for the further de-enrichment of the He ion flow impinging on the target, with respect to the one entering the divertor region, from 3.1% to 1.1% (cf table 1).

The stronger leakage of He ions towards upstream also increases the possibility that they are recycled at the main wall. The resulting flux amplification at the main wall (consistent with figure 9(*d*)) causes a feedback loop which decreases even more divertor recycling. This is made evident by comparing the relative intensity of divertor and main wall recycling for the two species. Whereas for deuterium the flux recycled at the divertor is roughly one order of magnitude larger than the one recycled at the main wall boundary, for helium the two quantities are similar in magnitude.

4.4. Influence of divertor closure and targets inclination

The net influx of atoms into the subdivertor recycling volume, from a given recycling source at the targets, is largely influenced by geometrical aspects [13, 79–81]. Retention of the recycled atoms in the subdivertor volume is better if the divertor plasma volume is closed, e.g. if the two regions are separated by a ‘roof baffle’, as the one present at AUG [82]. The

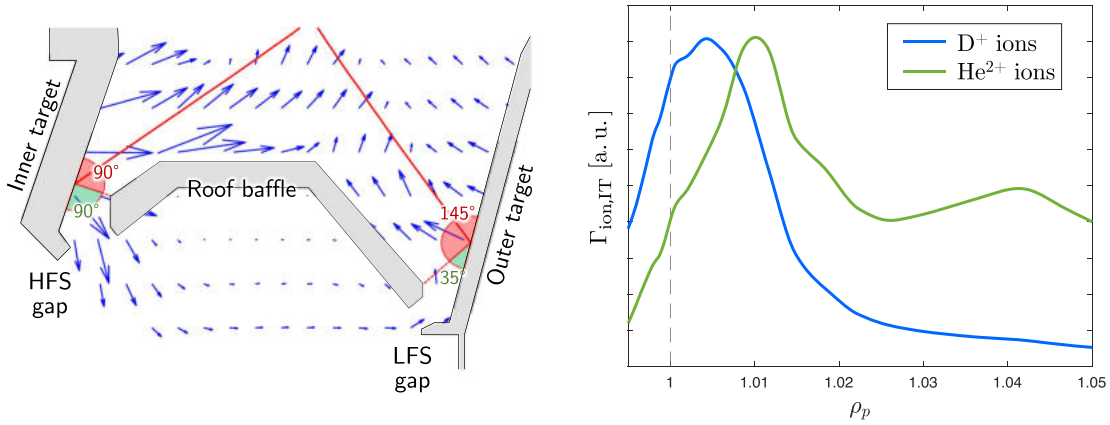

Figure 12. Left: simulated flow velocity field of the recycled He atoms, with arrow lengths representing the intensity of the He atom flux (i.e. its flux density). Right: simulated (normalized) parallel ion flux impinging on the inner target, for D^+ ions and He^{2+} ions.

effect is very similar to the one expected with the 'dome' planned for ITER [41]. In this case, the resulting subdivertor neutral density is proportional to the probability that the recycled atoms are directly emitted towards this region, rather than towards the 'hot' plasma. This is achieved if the location of maximum recycling along the targets (i.e. of maximum impinging ion flux) is close to the entrance to the subdivertor region (i.e. the gaps between targets and baffle). Additionally, the targets' inclinations plays also a role: whereas the neutrals reflected from the targets are re-emitted in a direction which mostly depends on the direction of the incident ions, the recycled ones are re-emitted according to a cosine distribution which peaks on the normal direction with respect to the target plates. Therefore, the angle between the target plate and the first-flight direction to the gaps influences the probability with which a recycled neutral can be directly scattered towards the gaps.

The left box in figure 12 visually shows the fluxes of the recycled He atoms in terms of flow velocity field. This shows that a net flux of He atoms leaves the divertor plasma region at the inner side, through the HFS gap. At the outer side, instead, a net flux re-entering the divertor plasma through the LFS gap is simulated, i.e. some He atoms from the subdivertor recycling volume are immediately recirculated towards the plasma. This can be explained noting that the separatrix strikes the inner target surface right in front of the HFS gap, while it strikes the outer target surface at some distance above the LFS gap. Therefore, it is easier for particles recycled from the inner target to be scattered towards the subdivertor volume, rather than particle recycled from the outer target. This is similar to what observed e.g. in [76].

The right plot in figure 12 shows that the location of maximum recycled flux from D^+ ions, along the inner target, is closer to the gap than from He^{2+} ions. Therefore a larger fraction of the recycled D atoms and molecules will reach the gaps. This explains the further de-enrichment of the neutral He density in the subdivertor recycling volume, with respect to the flux recycled from the targets, from 1.1% to 0.4% (cf table 1).

4.5. Overall contribution to the divertor compression

Globally, our simulation shows a strong de-enrichment of helium in the exhaust gas, with a relative concentration (with respect to the density of the main species) decreasing from 14.3% in the core to 0.4% in the subdivertor volume (cf table 1). This is qualitatively consistent with the experimental results [30, 70].

As we have shown, the processes determining this are mostly related to the physics of helium transport and recycling. With our analysis we assessed that such de-enrichment takes place gradually while travelling from core to divertor, with roughly similar contributions from processes taking place in the different plasma regions. The differences between helium and deuterium determining this situation are (i) a deeper ETB for helium, which is mainly caused by the higher ion charge, (ii) a lower parallel ion velocity in the SOL for helium, which is mainly caused by the collisional transport properties, and (iii) a higher ion leakage from the divertor for helium, which is caused by its higher first ionization energy. This emphasizes that the low simulated value of helium compression is caused by a complex interplay of processes whose net result is a weaker helium transport towards the divertor than that of deuterium.

4.6. Improvements to the default SOLPS-ITER physics model

Despite the understanding gained via the analysis described in the previous sections, the important underestimation of the simulated helium compression (i.e. 0.12) with respect to the experiment (i.e. 1.6), of a factor of more than 10, remains to be explained. We identified a series of possible improvements, mainly related to the modelling of divertor recycling, which can be achieved modifying the SOLPS-ITER physics-related input settings with respect to the default ones, described in the next subsections. These mostly modify the intensity of divertor recycling and the simulated interplay between the location of the stagnation surface of the

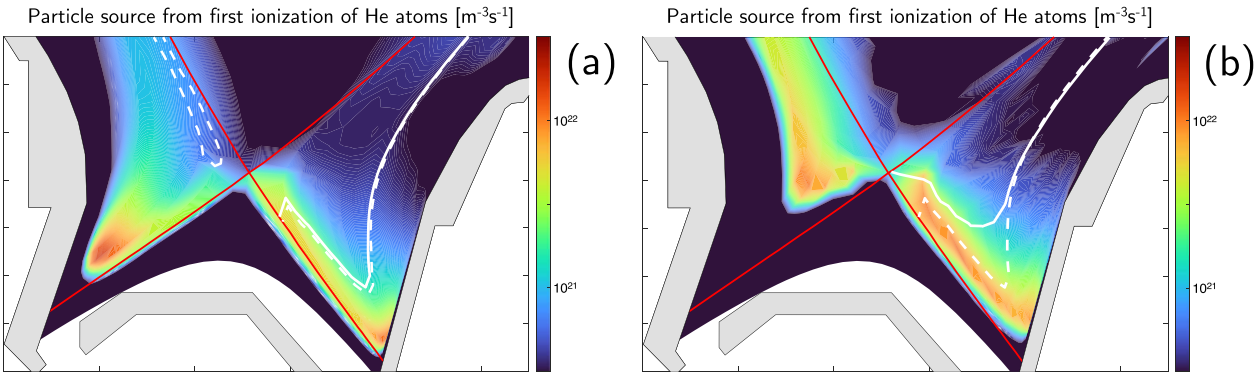

Figure 13. Change of the simulated divertor recycling for helium (in terms of ionization front and stagnation surface) when improving the SOLPS-ITER physics model. (*a*): changing the closure of the transport equations (stagnation surface as dashed while line for the default closure vs. solid white line for the Zhdanov-Grad closure). (*b*): activating the drift flows (stagnation surface as dashed while line without drifts vs. solid white line with drifts).

He ion flow and ionization front of the recycled He atoms (figure 13).

4.6.1. Role of improved parallel transport model. The default form of the parallel momentum balance equation for impurities used in SOLPS-ITER is the one derived from the original Braginskii equations and described in [77]. The coefficients describing collisional processes determine the parallel forces, in particular friction and thermal forces. These are analytically derived following a given closure for the fluid equations. The form of the coefficients used by default in SOLPS-ITER is the one derived in [83, 84]. This is valid for arbitrary impurity concentrations, but is calculated assuming a nearly zero mass ratio between main ions and impurity ions. Whereas this may be reasonable for heavier impurities, it is not accurate for the description of collisional He ion transport. Recently, improved coefficients valid for comparable masses of main and impurity ions were calculated and implemented in SOLPS-ITER [85]. The application of this improved closure was shown to alter the balance between friction and thermal forces, especially for light impurities [86].

Implementing the improved closure did not change the background plasma solution, but altered, as expected, the parallel force balance for He ions. This is shown in detail in the appendix A. This produced a small shift of the stagnation surface towards upstream (cf figure 13(*a*)). As a result, the fraction of recycled He atoms ionized in a region with forward He ion flow in the SOL increases from 58.4% (cf table 2) to 64.9%. Consequently, the He ion leakage from the divertor is reduced, and the simulated He compression increases from 0.12 to 0.16. This is consistent with the results presented in [86].

4.6.2. Role of neutral-ion collisions. As discussed in the section 3.2, several atomic reactions involving the collision of He atoms with plasma ions are not included by default in the Eirene reaction set. These may strongly impact the trajectories of the recycled He atoms, hence in turn where and how quickly these are ionized.

According to figure 4, at high plasma temperatures, for most of the recycled He atoms the first interaction with the plasma is an electron-impact ionization. In this case, these would undergo a ballistic trajectory from the recycling location until they are ionized. At less than 15 eV, the mean free path for CX collisions with He ions (i.e. the reactions $He^0 + He^+ \rightarrow He^+ + He^0$ and $He^0 + He^{2+} \rightarrow He^{2+} + He^0$) and elastic collisions with D ions (i.e. the reaction $He^0 + D^+ \rightarrow D^+ + He^0$) becomes shorter than the ionization one. This would cause multiple collisions for He atoms before the ionization. A region with sufficiently low temperature does exist, especially in the inner divertor, in our plasma solution (cf figure 6(*e*)). After activating these collisions, following a sufficiently high number of test particle trajectories simulated by Eirene, we calculated that He atoms recycled at the inner and outer targets undergo, on average, 0.07 and 0.03 CX collisions with He^+/He^{2+} ions per simulated trajectory, respectively. Therefore, the impact of these CX collisions is negligible, mainly because of the low He ion density in the simulated case. In the same way, we calculated that He atoms recycled at the inner and outer targets collide, on average, 6.10 times and 6.16 times with D^+ ions before being ionized, respectively. These elastic collisions are, therefore, dominant, transforming the motion of recycled He atoms from ballistic to diffusive.

CX collisions with D^+ ions (i.e. the reaction $He^0 + D^+ \rightarrow He^+ + D^0$), instead, do not cause the He atoms to be scattered, but remove one electron from them. The result is an additional 'effective' ionization mechanism. However, according to figure 4, the range in which these occur more likely than an electron-impact ionization (effectively increasing the ionization probability) is limited to very low temperatures, i.e. less than around 1.5 eV. After activating these collisions, following again a sufficiently high number of test particle simulated

by Eirene, we calculated that, out of all He atoms recycled from the inner and outer targets and ionized in the divertor plasma, the final collision was a He-D^+ CX collision only for the 0.05% and the 0.10% of these, respectively. Therefore, also the impact of CX collisions with D^+ ions is rather negligible, mainly because of the very low probability of the these to occur.

Implementing all neutral-ion collisions did not alter significantly the position of the ionization front of recycled He atoms, but caused a further slight increase of the simulated compression from 0.16 to 0.18. This is linked to an increased fraction of recycled He atoms which is directly scattered towards the subdivertor region, rather than towards the 'hot' plasma (cf section 4.4), as a result of increased collisions with D^+ ions: after activating these collisions, from the inner target this is fraction increased form 15.5% to 17.3%, while from the outer target it is increased from 1.9% to 2.4%.

We conclude that, although the mere presence of such collisions is dominant over ionizations, differently from what was previously believed [13], their impact on divertor compression remains limited, at least in the scenario investigated here.

4.6.3. Role of drift flows. Finally, a further, substantial change to the entire divertor plasma solution (cf figures 6(*d*) and (*e*)) is caused by the activation of the drifts flows ($\boldsymbol{E}\times\boldsymbol{B}$ and diamagnetic drifts). Different main ion flows, electron temperatures and parallel electron/ion temperature gradients drastically affect both the stagnation surface of the He ion flow and the ionization front of the recycled He atoms (cf figure 13(*b*)).

Fully activating the drift terms altered, in first instance, the parallel force balance for He ions. This is shown in detail in the appendix A. This produced a shift of the stagnation surface towards upstream at the LFS which is much more pronounced than that achieved by using improved parallel transport coefficients (cf figure 13(*b*)). The ionization front is also shifted towards upstream, especially in the inner divertor, because of a much lower temperature obtained when drifts are activated. However, at the HFS, there is no flow reversal both without and with drifts, so the impact of this on ion leakage is limited. Globally, the fraction of recycled He atoms ionized in a region with forward He ion flow in the SOL increases further to 68.8%. The He ion leakage from the divertor is further reduced, and the simulated He compression increases from 0.18 to 0.21.

4.6.4. Considerations. Adding the aforementioned additional pieces of physics, not included in the default SOLPS-ITER model, yielded a more realistic account of the divertor recycling of He atoms. This increased the simulated He compression by an overall factor of roughly 2 (i.e. from 0.12 to 0.21). Nonetheless, the simulated value remains almost one order of magnitude lower than in the experiment (i.e. 1.6). This suggests that additional physics components are still missing in SOLPS-ITER, which likely affect the treatment of the transport of He ions in the SOL. Possible reasons for this will be discussed in the section 6.2.

5. Characterization of subdivertor helium gas transport and pumping

This section discusses the second set of processes which, according to figure 1, determine the overall He particle balance, i.e. the transport and pumping of neutral He atoms in the subdivertor volume. Although the geometry of the subdivertor region, as considered by the Eirene triangular grid, is simplified, it preserves the complexity of the material structures present in reality. As such, we were able to model and interpret the phenomena which constitute and limit the overall conductance of the He gas flow towards the pumps.

A simple figure of merit for quantifying subdivertor helium gas transport is its subdivertor density ratio R_{He} (equation (2)). Starting from a given He atom density in the subdivertor recycling region, this parameter will quantify the efficiency with which He atoms are transported towards the pumping volume, from which they can be finally permanently removed from the vessel. This can be seen as the result of the interplay between multiple aspects:

- Physical obstacles encountered in the way from the recycling source to the pumping surface, such as vessel support structures, cables and diagnostics gauges in the subdivertor region, cause a resistance effect for the gas flow, obstructing its flow towards the pumps and determining a subdivertor density ratio larger than unity.
- Those recycled atoms which successfully enter the subdivertor region still have a chance to be reflected multiple times by the material boundaries of the vacuum vessel and recirculate towards the divertor plasma or the main chamber through physical gaps, hence be re-ionized. For maximizing the pumping, the entire subdivertor region should be sufficiently closed, e.g. through baffles.
- If the neutral gas density is large enough, collisions between the gas atoms/molecules are dominant over the collisions between the vessel walls, invalidating the assumption of free molecular flow. In this case, the flow is also limited by its own viscosity. In case of impurities, their flow is influenced by the viscosity of the main gas flow via friction.
- The intensity of the sink given by the active pumping not only governs the gas removal rate, but also influences the gas flow itself, if it is comparable to the intensity of the gas source within the same volume.

Figure 14 illustrates the He gas flow in the entire subdivertor volume, in form of streamlines.

Divertor recycling generates the flux of He atoms which constitutes the only net source of particles for the subdivertor region. Consistently with what already discussed in the section 4.4, figure 14 shows that a net flux of He atoms leaves the divertor plasma region at the inner side, through the HFS gap, while at the outer side a net flux entering the divertor

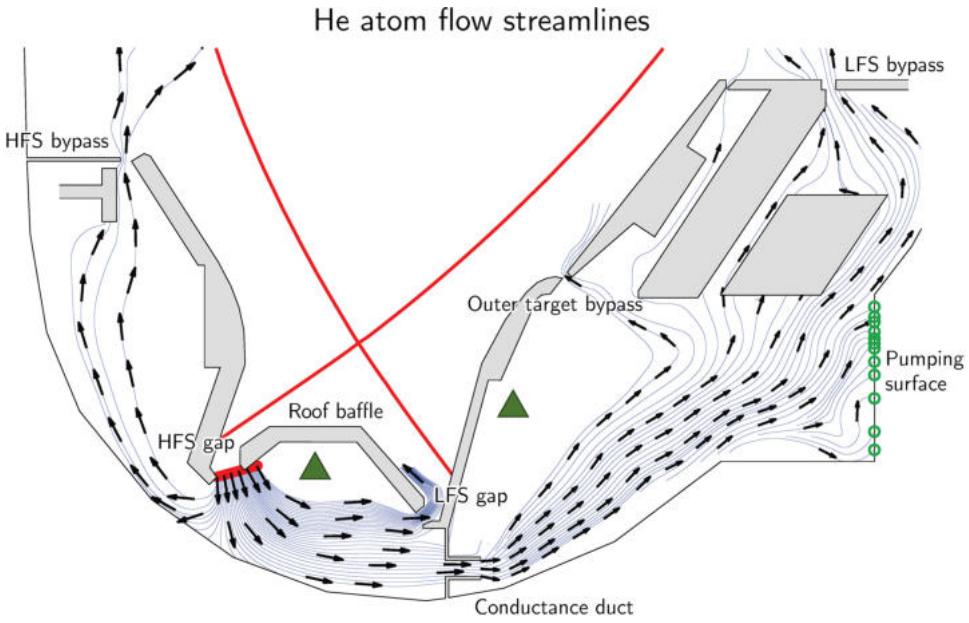

Figure 14. Streamlines of the simulated He atom flow, with starting point at the roof baffle HFS gap connecting divertor plasma volume and subdivertor region, following it until the various sinks (leakage path towards the divertor plasma volume through the roof baffle LFS gap, leakage paths towards the main chamber through the HFS and LFS main chamber baffle gaps and outer target gap, and absorption from the pumping surface representing the pump duct). The green triangles represent the locations, within the recycling and pumping volumes, from which the simulated He densities, as mentioned in the text and in the table 4, are extracted.

plasma through the LFS gap is simulated. Therefore, some He atoms from the subdivertor recycling volume are immediately recirculated towards the divertor plasma before even reaching the pumping volume. A further, non negligible fraction of the He atom flux which reaches the pumping volume is still recirculated to the divertor plasma or to the main chamber, despite the presence of baffles at the HFS and at the LFS of the vacuum vessel.

As a result, only a small fraction of the entire gas influx within the subdivertor region is pumped. Following a sufficiently high number of test particle trajectories simulated by Eirene, we calculated that, out of all He atoms generated from divertor recycling, only around 2.1% get pumped, while the remaining 97.9% re-enter in some way the plasma and get ionized. In the following subsections, the processes determining this situation will be analyzed.

5.1. Subdivertor conductance model

A key aspect required for a realistic simulation of neutral gas flows towards the pumping surfaces concerns the resistance created by physical obstacles encountered on the way. This causes a pressure drop for the gas flow, which is not favourable for the pumping as it implies a lower pressure in front of the pumping surfaces. For the case of the AUG geometry, this effect can be quantified in terms of the subdivertor density ratio. For a deuterium gas, at divertor pressure levels typical of H-mode plasma discharges (i.e. of the order of one to few Pa), a ratio of around 4−5 is usually observed between the densities in the two volumes (cf section 2.3). This value is observed to increase with increasing pressure, likely because the flow is further limited by the increased D_2 gas viscosity. For the case of helium, this quantity has not been directly measured, because of the lack of an operating Penning gauge in the recycling volume. The empirical considerations reported in the section 2.3 led us to assume a ratio of around 1.75 for the helium gas. This is smaller than the measured one for D_2 molecules because of the lack of the strong cryopumping sink for He atoms.

To support this assumption, we employed a neutral gas conductance model in our computational grid. This allows to emulate the resistance due to physical obstacles using a fictitious duct which separates recycling and pumping volumes (cf figure 14). The conductance $\mathcal{L}$, measured in $\mathrm{m}^{-3}\,\mathrm{s}^{-1}$, induced by this duct, allows to relate the density difference between the upstream and downstream reservoirs to the flux Γ flowing between the two via the equation

$$\Gamma = \mathcal{L} \cdot (n_{\mathrm{up}} - n_{\mathrm{down}}) . \tag{6}$$

Appendix B describes in more detail the employed conductance model. The theoretical free molecular conductance for 4 AMU particles predicted by such model is 45 $\mathrm{m}^{-3}\,\mathrm{s}^{-1}$.

In case of free molecular flow, for different gas masses, the conductance should scale with the square root of the mass ratios. He atoms and D_2 molecules have nearly the same mass, and the resistance exerted by the physical obstacles in the subdivertor region on the gas flow is the same for all neutral gas species. Therefore, if such a structure correctly emulates the pressure drop for the D_2 flow, it will then correctly emulate also the pressure drop for the He flow, provided that other processes affecting the flow (e.g. neutral-neutral collisions)

Table 3. Simulated net particle fluxes flowing into and out from the entire subdivertor region, balancing according to equation (7). Given in the table are the atomic fluxes (i.e. the D_2 particle flux component is accounted twice), flowing through the various gaps/bypasses/pumping surfaces, in s^{-1}. For the fluxes leaving the subdivertor region (i.e. negative), the fraction with respect to the only positive flux (i.e. the inflow from the divertor plasma volume through the HFS gap) is given. The pumped flux corresponds to the total gas source into the simulation.

	HFS gap (inflow)	LFS gap (outflow)	$\sum$ leaks to divertor plasma vol.	$\sum$ leaks to main chamber	Pumped flux
$D+D_2$	$+10.80 \cdot 10^{21}$	$-0.53 \cdot 10^{21}$ (4.9%)	$-0.66 \cdot 10^{21}$ (6.1%)	$-4.77 \cdot 10^{21}$ (44.2%)	$-4.84 \cdot 10^{21}$ (**44.8%**)
He	$+8.02 \cdot 10^{19}$	$-2.63 \cdot 10^{19}$ (32.8%)	$-1.17 \cdot 10^{19}$ (14.6%)	$-3.81 \cdot 10^{19}$ (47.5%)	$-0.41 \cdot 10^{19}$ (**5.1%**)

are taken into account. In our main simulation, with activated neutral-neutral collisions, the simulated He atom flux through this duct $\Gamma_{\mathrm{He,rec}\rightarrow\mathrm{pump}}$ is $2.33 \cdot 10^{19}$ s^{-1}, and the simulated densities in the recycling and pumping volumes are $n_{\mathrm{He,rec}} = 5.78 \cdot 10^{17}$ m^{-3} and $n_{\mathrm{He,pump}} = 3.41 \cdot 10^{17}$ m^{-3}. The row (*b*) in figure 15 shows the simulated distribution of the He atom density in the entire subdivertor region, for the base case. The simulated subdivertor density ratio R_{He} is, therefore, 1.70. This provides an *a posteriori* confirmation of our assumption for such ratio, which was necessary because of the availability of He atom density measurements only in the pumping volume but not in the recycling volume (cf section 2.3).

According to equation (6), the real conductance $\mathcal{L}_{\mathrm{He,rec}\rightarrow\mathrm{pump}}$ is therefore 98 $m^{-3}\,s^{-1}$. The much higher value with respect to the analytically calculated one can be attributed to the effect of neutral-neutral collisions. At the simulated He atom densities, the mean free path of He-He collisions is of the order of tens of m (cf figure 5). Therefore, these do not play any role, and He gas flow is not limited by its own viscosity. However, given the simulated background D_2 density in the range $5 - 10 \cdot 10^{19}$ m^{-3}, the mean free path of D_2-D_2 and D_2-He collisions is of few cm (cf figure 5), which is lower than the characteristic dimension of the volumes in the subdivertor region. Therefore, these collisions take place more frequently than the collisions of He atoms with the material surfaces, invalidating the assumption of free molecular flow. The D_2 gas flow is, therefore, limited by its own viscosity [87–89]. Since it is much more intense than the He gas flow, because of the higher density and additional cryopump sink, the entrainment of the He gas flow into the D_2 gas flow via inter-species friction results in a drag effect. This explains the higher conductance with respect to analytical prediction in case of free molecular flow.

5.2. He gas dynamics and recirculation

A global particle balance on the region can be performed to quantify the impact of recirculated fluxes over the pumped flux:

$$\Gamma_{\mathrm{inflow,HFS\ gap}} = \Gamma_{\mathrm{outflow,LFS\ gap}} + \sum \Gamma_{\mathrm{leaks,div.}} + \sum \Gamma_{\mathrm{leaks,main}} + \Gamma_{\mathrm{pumped}}. \quad (7)$$

Namely, consistently with figure 14, the flux of neutral particles entering the subdivertor region through the HFS gap must equate the flux re-entering the divertor plasma region through the LFS gap, plus the fluxes leaking to the divertor plasma region through the outer target bypass, plus the flux leaking to the main chamber through the HFS and LFS bypasses, plus the pumped flux. For a better understanding of the neutral gas dynamics in this region, we calculated the various terms of equation (7) across the flow domain. Table 3 shows the various terms of the balance, found by extracting the fluxes crossing transparent surfaces placed in the Eirene grid corresponding to the various gaps/bypasses, for deuterium (D atoms + D_2 molecules) and helium.

For the deuterium gas, the recirculated flux is comparable to the pumped flux (which is 44.8% of the total inflow). Most of the flux is leaked towards the main chamber, rather than towards the divertor plasma volume. For helium, instead, the pumped flux is only 5.1% of the total inflow. This is easily motivated by the much reduced pumping applied to He atoms, which are not captured by the cryopump. However, a comparable fraction of the total inflow, as for deuterium, is leaked towards the main chamber. The increased terms for helium are the fluxes leaked towards the divertor plasma volume, especially towards the LFS gap. This is consistent with the reduced flux of He atoms from the recycling volume to the pumping volume, caused by the absence of the cryopumping sink for them. He atoms tend, in this way, to remain longer within the recycling volume, which favours leakage towards the divertor plasma volume through the LFS gap (cf section 4.4).

5.3. Impact of neutral gas friction on the helium atom flow

As already mentioned in the section 5.1, neutral-neutral collisions are seen to influence the He atom flow from the subdivertor recycling volume to the pumping volume, via friction with the much more intense D_2 flow.

Figure 15 shows the simulated He atom density and the He atom flow velocity field, in the entire subdivertor region, in the base case, i.e. with neutral-neutral collisions all activated (row (*b*)), and in a case in which we deactivated only the D_2-He collision (row (*a*)). The He ion density at the plasma midplane is kept the same through the core boundary conditions. As a result of the unchanged plasma conditions with regard to He ions, the recycled flux from the divertor targets is roughly the same in the two cases.

The simulated He atom density in the subdivertor recycling volume is, however, different. He atoms are uniformly distributed in the case without D_2-He collision, as a result of their pure free molecular flow (with He-He and D-He collisions

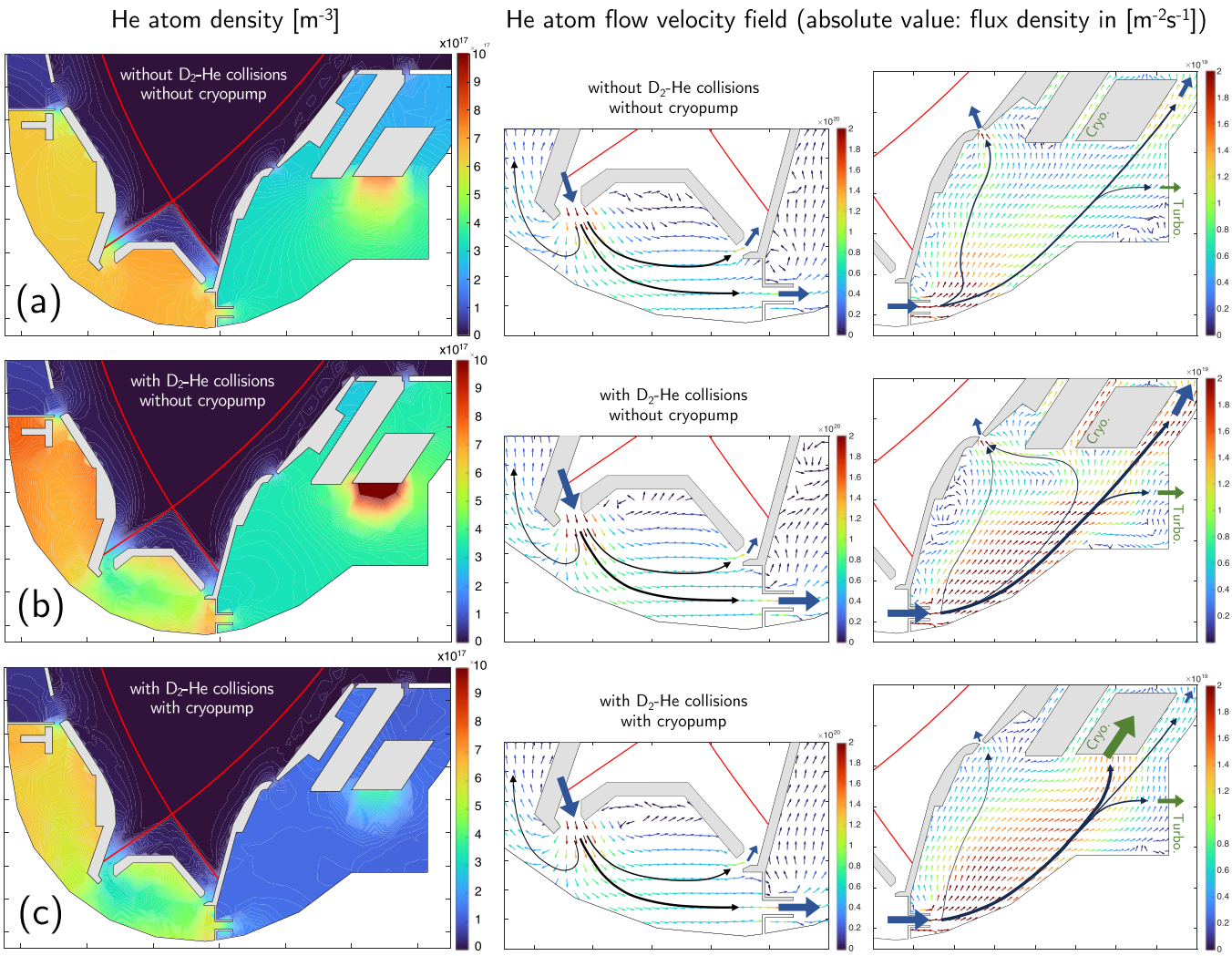

Figure 15. Distribution of the simulated neutral He atom density in the entire subdivertor region and simulated He atom flow velocity field (with color scale indicating the absolute flux density), for different cases. Row (*a*): deactivated D_2-He elastic collisions and cryopump ineffective for He atoms. Row (*b*): activated D_2-He elastic collisions and cryopump ineffective for He atoms (corresponding to the base case). Row (*c*): activated D_2-He elastic collisions and cryopump effective for He atoms, i.e. imposing the same capture coefficient as for D_2 molecules. The black arrows qualitatively represent the flow streamlines.

being negligible). Activating the D_2-He collisions, the distribution of He atoms in this volume is not uniform anymore, and their average density is decreased by a factor of roughly 30%. The cause is the enhancement of the flux towards the pumping volume, driven by the friction exerted by the more intense D_2 flow.

In the pumping volume, the simulated He ion density is roughly unchanged. This means that also the subdivertor density ratio (equation (2)) is decreased by roughly 30% with respect to the case without D_2-He collisions. The simulated He atom flow velocity field in this volume is, however, strongly impacted. In the case without D_2-He collisions, the He atom flow, which enters the volume through the conductance duct, splits in two distinct currents, one travelling towards the pumping surface and one travelling towards the outer target bypass. In the case with D_2-He collisions, instead, the He atom flow is more intense and is preferentially directed towards the pumping surface, and the flow current to the outer target bypass is weaker. This is caused by the friction exerted by the strong D_2 flow, which is mainly directed towards pumping surfaces. Therefore, although the applied pumping speed on He atoms is unchanged, the enhanced flow of He atoms towards the turbopump surface causes an increase of capture rate from this, and therefore also of the pumped He flux. As a side effect, the He atom flow towards the LFS bypass (which is behind the cryopump) is also enhanced. Therefore, the leaked flux towards the main chamber also increases.

The impact of the friction exerted by the D_2 flow clearly depends on the background D_2 pressure, since for low pressures D_2-He collisions would occur less often. To assess this, we performed a further set of simulations with varying D_2 gas puff, so as to achieve different D_2 pressure levels in the subdivertor region. In these simulations, the He ion density at the plasma midplane is still kept constant. Table 4

Table 4. Change in the transport of He atoms towards the pumps, at different pressures of the background D_2 gas measured in the recycling volume, without and with D_2-He collisions activated. From left to right: He atom densities in the recycling and in the pumping volumes in the subdivertor region (i.e. green triangles in figure 14); He atom flux from the recycling to the pumping volume, and resulting conductance; Pumped flux of He atoms.

p_{D_2}	(D_2-He)	$n_{He,rec}$ (m^{-3})	$n_{He,pump}$ (m^{-3})	$\Gamma_{He,rec\rightarrow pump}$ (s^{-1})	$\mathcal{L}_{He,rec\rightarrow pump}$ ($m^{-3}\,s^{-1}$)	$\Gamma_{He,pumped}$ (s^{-1})
0.10 Pa	no	$4.51\cdot10^{16}$	$2.01\cdot10^{16}$	$1.05\cdot10^{18}$	42	$1.40\cdot10^{17}$
	yes	$3.71\cdot10^{16}$	$1.90\cdot10^{16}$	$1.07\cdot10^{18}$ (**+1.9%**)	59	$1.46\cdot10^{17}$ (**+4.2%**)
0.35 Pa	no	$3.29\cdot10^{16}$	$1.55\cdot10^{16}$	$0.76\cdot10^{18}$	43	$1.11\cdot10^{17}$
	yes	$2.30\cdot10^{16}$	$1.53\cdot10^{16}$	$0.93\cdot10^{18}$ (**+22.4%**)	120	$1.26\cdot10^{17}$ (**+13.5%**)
0.55 Pa	no	$4.11\cdot10^{16}$	$1.88\cdot10^{16}$	$0.94\cdot10^{18}$	43	$1.36\cdot10^{17}$
	yes	$2.89\cdot10^{16}$	$1.91\cdot10^{16}$	$1.26\cdot10^{18}$ (**+34.0%**)	129	$1.65\cdot10^{17}$ (**+21.3%**)
0.70 Pa	no	$5.54\cdot10^{16}$	$2.53\cdot10^{16}$	$1.26\cdot10^{18}$	42	$1.77\cdot10^{17}$
	yes	$4.12\cdot10^{16}$	$2.56\cdot10^{16}$	$1.74\cdot10^{18}$ (**+38.1%**)	112	$2.28\cdot10^{17}$ (**+28.8%**)
0.80 Pa	no	$8.64\cdot10^{16}$	$3.67\cdot10^{16}$	$1.97\cdot10^{18}$	40	$2.63\cdot10^{17}$
	yes	$7.22\cdot10^{16}$	$3.95\cdot10^{16}$	$2.88\cdot10^{18}$ (**+46.2%**)	66	$3.53\cdot10^{17}$ (**+34.2%**)

shows how the simulated He densities and fluxes vary over a D_2 pressure range spanning 10^{-1} to 1 Pa, which is typical of low-to-medium-density H-modes at AUG. The effect of the D_2-He friction is best visible in the percentage increase of the He flux from the recycling volume to the pumping volume and of the pumped He flux when activating the D_2-He collisions.

At the lowest simulated D_2 pressure the impact of D_2-He collisions on the simulated He atom flux $\Gamma_{He,rec\rightarrow pump}$ from the recycling volume to the pumping volume is limited. Therefore, He atoms are still very weakly entrained into the D_2 flow. Consequently, also the increase of the pumped flux $\Gamma_{He,pumped}$ is limited. Towards the highest simulated D_2 pressure, instead, $\Gamma_{He,rec\rightarrow pump}$ is roughly 46% larger than in the case without D_2-He collisions. This is caused by the stronger entrainment into the D_2 flow. As a result, $\Gamma_{He,pumped}$ is roughly 34% larger. Noticeably, the relative increase of $\Gamma_{He,pumped}$ is lower than the relative increase of $\Gamma_{He,rec\rightarrow pump}$ (apart from the lowest pressure case). This is caused by the concurrent increase of the leaked flux towards the main chamber through the LFS bypass.

We also calculated the resulting conductances $\mathcal{L}_{He,rec\rightarrow pump}$ between the two subdivertor volumes, from the simulated He atom density difference in the two volumes and the simulated He atom flux, according to equation (6). As expected, $\mathcal{L}_{He,rec\rightarrow pump}$ does not change with increasing D_2 pressure in the simulations without D_2-He collisions, as the He atom flow is not influenced by the D_2 flow. The simulated values (between 40 and 45 $m^{-3}\,s^{-1}$) are in very good agreement with the theoretical prediction for a free molecular flow (cf appendix B). With activated D_2-He collisions, instead, $\mathcal{L}_{He,rec\rightarrow pump}$ is always higher than the free molecular expectation. However, the trend is not monotonous, as this has a maximum at the 'intermediate' simulated D_2 pressure. This is due to the fact that, whereas the entrainment of He atoms into the D_2 flow constantly increases with the D_2 pressure, the conductance of the D_2 flow itself decreases towards higher D_2 pressure, being this more and more limited by its own viscosity [87–89]. The combination of the two effects explains the calculated trend of $\mathcal{L}_{He,rec\rightarrow pump}$.

In summary, the activation of neutral-neutral collisions in our simulations led us to conclude that the impact of D_2-He friction on the He gas flow (and, more importantly, on the pumped He flux), is clearly visible, but not dramatic. Even in case of full entrainment of He atoms within the D_2 flow, which would be achieved at pressures of the order of several Pa or higher, this would not overrule the bad pumping of He atoms caused by ineffectiveness of the cryopump for them.

5.4. Impact of active pumping on the helium atom flow

The impact of active pumping, through pumping surfaces defined within the Eirene grid, can be seen not only on the gas removal rate (which affects the global source/pump balance in a coupled B2.5-Eirene run), but also on the simulated gas flow itself. This can be seen e.g. by comparing the simulated density and flow velocity of He atoms in the base case (row (*b*) in figure 15), where the only pumping sink for He atoms is given by the turbopumps surface, to a case (row (*c*) in figure 15) in which we set the same capture coefficient for D_2 molecules on the cryopump surface. Again, the He ion density at the plasma midplane is kept the same, resulting in an equal recycled flux from the divertor targets in the two cases.

In the case with cryopump fully effective on capturing He atoms, the He atom flux travelling from the subdivertor recycling volume to the pumping volume is mostly unchanged, and only slightly increased. Within the pumping volume, however, the strong additional sink at the cryopump surface causes the flow to be preferentially directed towards this, strongly reducing the intensity of the flow currents directed towards the outer target and the LFS bypasses. Consequently, the pumped flux is increased, at the expense of the leaked flux towards the divertor plasma volume and the main chamber.

Within the recycling volume, the fact that the outflow (through the conductance duct) is only slightly increased, with the inflow (from divertor recycling) being the same, causes the simulated He atom density to be only slightly reduced. As a consequence, the simulated divertor compression is also

Table 5. Calculated net particle fluxes flowing out from the subdivertor region (in terms of fraction with respect to the influx from the HFS gap), divertor compression, subdivertor density ratio and He ion concentration at the plasma midplane ($n_{He^{2+}}/n_{D^+}$ at the pedestal top) in simulations performed at different levels of cryopump effectiveness for He atoms. These simulations are performed with fixed and equal He gas puff.

Cryo. effectiveness for He atoms	% leaked flux (div. plasma vol.)	% leaked flux (main chamber)	% pumped flux (turbo. + cryo.)	C_{He}	R_{He}	f_{He} (plasma midplane)
Off ($C_{capture,He} = 0.00$)	47.4%	47.5%	**5.1% + 0.0%**	0.12	1.70	**0.143**
1/4 ($C_{capture,He} = 0.05$)	38.4%	40.7%	**3.4% + 17.5%**	0.12	2.38	**0.047**
1/2 ($C_{capture,He} = 0.10$)	35.0%	36.0%	**2.6% + 26.4%**	0.11	2.99	**0.033**
3/4 ($C_{capture,He} = 0.15$)	33.0%	33.1%	**2.1% + 31.8%**	0.11	3.56	**0.028**
Full ($C_{capture,He} = 0.20$)	31.8%	31.4%	**1.7% + 35.1%**	0.11	4.09	**0.025**

very similar. This confirms that, whereas the applied pumping speed affects the simulated impurity concentrations by altering the global source/pump balance, it does not directly have a strong impact on how efficiently impurities are transported towards the divertor targets from the plasma, and thereby recycled. The latter aspect mostly depends on transport phenomena on the plasma side, as pointed out in the section 4, and is therefore conceptually distinct from the pumping-related aspect of impurity exhaust. This is also in line with what was observed in previous modelling works [90], and consistent with reduced models describing impurity exhaust [91].

The two simulations described in the rows (*b*) and (*c*) of figure 15 feature an identical concentration of He atoms at the plasma midplane, as a fixed boundary condition. This allowed to focus on how the subdivertor He gas transport changes between the two cases. Since the pumped flux is much larger in the case with cryopump active, the net external source of He atoms in the plasma is also accordingly increased, to maintain the He ion density in the plasma unchanged. In order to evaluate how much an increase of the applied pumping speed affects the He concentration in the plasma, we performed further simulations with fixed external source and varying capture coefficient at the cryopump surface. This is increased from 0.00 (i.e. as in the base case) to 0.20 (i.e. the same as for D_2 molecules). Table 5 shows the simulated results.

Not surprisingly, the increase of intensity of the strong cryopumping sink in the pumping volume causes an increase of the fraction of the He atom flux entering the subdivertor volume which is pumped, and a decrease of the fraction which is leaked towards both divertor plasma volume and main chamber. As already discussed, the simulated He compression is only weakly affected, while the subdivertor density ratio increases to levels comparable to those observed and simulated for the D_2 gas, i.e. around 4 (cf section 2.3) with cryopump fully effective on He atoms. Most importantly, the He ion concentration at the plasma midplane strongly decreases, going from roughly 14% with cryopump fully off to roughly 2% with cryopump fully on. Its decrease is, however, non linear with increasing capture coefficient. This emphasizes how much the employment of efficient pumps can contribute to keep the He ion concentration in the plasma within tolerable values, even beyond the (still necessary) plasma and divertor scenario optimization. On the other hand, the substantial leakage towards the main chamber, which is still present also in the case with cryopump fully on, highlights that closing the subdivertor geometry might also be a key for optimize the pumping.

6. Discussion and possible further improvements

6.1. Implications for future devices

Important implications for the operation of future devices follow from our results. Because of several aspects intrinsic to its physical behavior, conventional divertors struggle in compressing helium. The resulting enrichment (i.e. the ratio between impurity compression and main species compression) is the worst among all recycling impurities [70], and its value is consistently below unity.

The experimental results documented in [30] and the numerical results from this work are in qualitative agreement with earlier experimental [18–20] and numerical [90] studies, performed at AUG with different divertor geometry and wall material. This is a further indication that helium transport and recycling mostly depends on the plasma scenario, and only in minor part on the technical characteristics of a specific device. This justifies a reasonable extrapolation of the observed behavior towards future reactors. In particular:

- In terms of edge transport (cf section 4.1), the desired good energy confinement in a reactor translates in a good particle confinement. The presence of an ETB, therefore, will constitute a first bottleneck for the flush-out of He ions from the confined region [8]. The lower pedestal collisionality foreseen in future reactors will, however, cause a significantly different impurity transport in the edge from the one observed in AUG [92, 93]. The impact of this on He compression is, currently, unclear.
- In terms of SOL transport (cf section 4.2), the balance between the predominantly collisional parallel transport and the predominantly turbulent radial transport of He ions will be also constrained by requesting plasma conditions for the SOL which are compatible with a high separatrix density and a highly recycling divertor [94].

- In terms of divertor recycling (cf section 4.3), the interplay between stagnation surface of the He ion flow and ionization front of recycled He atoms will also be determined by the desired divertor plasma scenario, which is constrained by the requirements of power exhaust (e.g. low temperature) [95]. Therefore, this is also not easily controllable independently. The physical dimensions of the divertor plasma volume, which will be larger and denser in future reactors [96], might however favour divertor retention of recycled He atoms, e.g. reducing their penetration at a given plasma temperature.
- In terms of geometric aspects (cf section 4.4), closure of the divertor plasma volume and favourable inclination of the targets plates are the only aspects determining the He compression which can be controlled. This can be done planning the presence of a roof baffle, positioning the separatrix strikelines close to the entrance of the subdivertor region, and tilting the targets so to maximize a direct scattering of the recycling He atoms towards it [15, 19]. These features are, indeed, already planned for the ITER divertor [27, 28]. An even further improvement might be given, in this regard, by non-conventional (e.g. long-legged) divertors.

These observations show that the room for optimization of helium transport and recycling in a reactor is limited. Any operational plasma scenario is indeed constrained by the requirements of core confinement and power exhaust [94, 97], which must be achieved simultaneously with those of helium exhaust.

The most relevant room for optimization of helium exhaust is therefore given by a proper design of the pumping systems. Extrapolating our results towards a reactor shows the unlikelihood of fulfilling the requirements of a stationary burning plasma only employing turbomolecular pumps, because of their limited pumping speed. It is, however, possible to design cryopumps which actively capture He atoms. For example, coating their surface with a sorbent like activated charcoal [98] or employ argon spraying to form a frosted cryotrapping layer [99]. The use of cryopumps capable of capture He atoms is, indeed, already planned for ITER [100, 101]. Steady-state operations such as the ones foreseen for DEMO will need instead more advanced approaches, such as multi-staged cryopumps or metal foil pumps [102].

6.2. Accuracy of edge transport models for impurities

Another important result of our work is the difficulty encountered by SOLPS-ITER in reproducing the experimentally measured He compression. This might constitute a serious drawback for the use of the code to predict the behavior of helium (as well as of other radiating impurities) in future fusion reactors. As already discussed, the reason for the observed discrepancy in our simulations is likely related to the treatment of helium transport itself, rather than to the general simulation fidelity (i.e. the simulated plasma background).

First of all, our results suggest that the simulated impurity densities in regions even far from the plasma core (e.g. in the neutral exhaust gas) are very sensitive to the choice of the radial transport coefficients inside the separatrix (cf section 4.1). This happens because the ion flux crossing the separatrix depends on the ion density gradient in the plasma edge. Therefore, the choice of radial transport coefficients for impurity species should always be carefully made, especially in H-modes where the presence of an ETB reduces the transport to neoclassical levels, i.e. making it strongly charge-dependent [8]. Nonetheless, in most of the already published SOLPS modelling works, to the best of the authors' knowledge, the particle diffusivity within the ETB for impurity species is very often kept the same as the one for the main species, even in predictive simulations in view of future reactors [103, 104]. This may be a wrong assumption, and may lead to misleading results.

Additionally, we found a non negligible impact on divertor recycling due to physical processes which can be modelled by SOLPS-ITER, but are not activated by default. Namely, an improved parallel momentum balance for impurities (cf section 4.6.1), atomic reactions beyond the simple electron-impact ionization, such as ion-neutral collisions (cf section 4.6.2), and drifts effects (cf section 4.6.3). The role of the drifts is consistent with what is already known [60, 62]. The role of ion-neutral collisions on transforming the ballistic trajectories of recycled impurity atoms into a diffusive motion is, however, more relevant than what was thought in the past [13]. Their impact on our simulated He compression is limited, as the investigated scenario is a moderately attached divertor in a medium-sized device. In denser and colder plasmas, as foreseen for future reactors, the impact of these might be much more pronounced. We recommend therefore to consider these aspects in both future interpretative and predictive studies involving edge transport simulations of impurities.

Nevertheless, the simulated He compression in our modelling still remains almost one order of magnitude lower than the experimentally measured one (cf section 4.6.4). We speculate that the difficulty encountered by SOLPS-ITER in this regard might be linked to physics components missing or not easily reproducible in its context. In particular:

- The anomalous transport coefficients for He particle transport in the SOL are the same as for the main species. This might not be an accurate assumption, although no experimental measurements exist to justify a different radial SOL transport for He (as well as for other impurities) with respect to that of hydrogenic species.
  Performing several exploratory simulations we observed that the simulated He compression can be increased by several units applying a lower particle diffusivity in the SOL for He^{+} and He^{2+}. This would bring the simulated value much closer to the experimental one. Optimizing this might help in achieving more accurate interpretative simulations. However, information on the radial SOL transport of He

ions in future devices would still be missing from predictive simulations.

- Fluid transport models cannot take into account MHD events, which might strongly affect edge transport. In particular, edge localized modes (ELMs) have been shown to effectively flush impurities out of the core [8, 105]. This happens because of two reasons: (i) the explosive ejection of ions across the separatrix at the ELM onset because of the pedestal relaxation [73, 106, 107], and (ii) the intense parallel free-streaming motion of ions within ELM filaments along the SOL towards the divertor [108, 109]. These processes are completely absent in our modelling, although the simulated discharge features type-I ELMs. Whereas the simulated radial plasma (figures 6(*a*)–(*c*)) and He^{2+} (figure 8(*b*)) profiles in the edge match inter-ELM measurements, the Penning gauge measurements are results of averaging more ELM cycles. Therefore, what we could measure is merely an 'ELM-averaged' He compression, while the simulated one should represent an 'inter-ELM' He compression.

  The simple multi-reservoir model described in [30], used to model the same AUG discharge investigated here, did emulate the impact of ELMs. It showed that, with otherwise same input parameters, ELMs alone can, as expected, increase the simulated He compression by several units. Similarly, other MHD models have shown that impurities are, indeed, ejected more efficiently from the plasma edge during ELM events [110].

  Implementing an ELM model also within SOLPS-ITER would be challenging, but not impossible. The increased separatrix flux at the ELM onset might be emulated by imposing a time-dependent modulation of the anomalous transport coefficients at the edge [111]. On the other hand, appropriate transient boundary conditions and flux limiters may mimic the kinetic effects impacting parallel SOL transport within ELM filaments [112].

The key for explaining the strong underestimation of He compression in SOLPS-ITER might, therefore, lie in a combination of the aforementioned deficiencies in its physics model.

Other advanced numerical models can also be used to confirm or contradict our speculations. For example, edge fluid turbulence codes such as GRILLIX [113] might be further developed to assess the impact of turbulence on impurity transport in the SOL [114]. On the other hand, non-linear extended MHD codes such as JOREK [115, 116] might be used to assess the impact of ELMs on impurity transport [117].

As a final remark, we stress that the discovery of the mismatch between model and experiment was made possible by the accurate Penning gauge measurements in the in-vessel exhaust gas at AUG [36], which so far are only available for helium. It is possible that the same mismatch exists for other impurities. All available numerical studies involving impurity transport (such as [65–68]) and impurity compression (such as [118]) are, however, not contrasted against experiments. We suggest to extend experimental validation activities of SOLPS-ITER, as far as possible, also towards impurities, and also in devices other than AUG.

7. Summary and outlook

Understanding the physics mechanisms determining helium exhaust is fundamental to develop operational scenarios for burning plasmas and assess their compatibility with the requirements of core confinement and power exhaust [94, 97]. Additionally, it supports the choice of wall materials and geometry for the plasma-facing components and the design of the pumping systems in future fusion reactors [119, 120].

For this purpose, we used the SOLPS-ITER code package to model a He-seeded deuterium H-mode discharge from the AUG tokamak [30], where the He concentration was diagnosed both in the plasma through CXRS [33, 35] and in the in-vessel exhaust gas through an optical Penning gauge [36]. Our modelling work aimed to interpret the experimental observations and identify the most important underlying physics mechanisms.

We observed, both experimentally and numerically, a reduced compression of He atoms in the subdivertor region, with respect to that of D_2 molecules. This indicates a poor He enrichment. This is determined by several physics aspects, including: (i) a deeper ETB for He ions than for D ions, which causes an increased core He confinement, (ii) a lower parallel velocity in the SOL for He ions than the one for D ions, which causes a reduced transport of He ions towards the divertor, and (iii) a higher first ionization energy of He atoms than of D atoms, which causes a reduced He retention in the divertor. Helium compression is therefore mostly related to the plasma conditions in a given scenario, rather than on the technical characteristics of a single device. As such, it represents a suitable parameter in terms of extrapolations towards future devices. Our results suggest therefore to carefully evaluate how much future reactor scenarios can tolerate such poor levels of He enrichment, in terms of compatibility with fuel dilution and stationary burning.

On the other hand, we also observed a non efficient transport of He atoms towards the pumps, with a pumped flux which is much lower than the flux leaking towards divertor plasma volume and the main chamber. This is, however, merely linked to the AUG pumping systems, where the installed cryopump cannot capture He atoms. At the neutral pressure levels characteristic of AUG H-modes, inter-species friction does play a role in dragging He atoms towards the pumps, driven by the stronger D_2 flow, thus enhancing the pumped flux. However, this role is minor with respect to the role played by vessel geometry, material structures in the subdivertor region and applied pumping speed. As such, the poor helium pumping capability of AUG, if extrapolated towards a reactor, would likely be incompatible with the requirements of a burning plasma [1, 2]. This emphasizes the importance of an adequate design of the pumping system for future reactors.

Strong quantitative discrepancies of the simulations with respect to the experiment are present, in terms of an important

underestimation of the experimentally measured He compression. The simulation fidelity relatively improved by activating non-default options in the SOLPS-ITER physics model (i.e. an improved closure scheme of the transport equation, ion-neutral collisions involving He atoms and drifts flows). Nevertheless, a discrepancy of almost a factor of 10 remains. This discrepancy is much more visible for helium than for the main plasma species. Further efforts should be therefore devoted to improve the physics model of SOLPS-ITER, especially for the transport of impurities and, in general, non hydrogenic species. The inclusion of self-consistent modelling of turbulence in the SOL and edge-localized MHD events might be of paramount importance. In absence of these, the predictive capability of SOLPS-ITER towards future devices with regards to impurity transport might not be guaranteed.

Our results emphasize the importance to benchmark the simulation results against impurity seeding experiments, and in which measurements from both plasma edge and neutral gas are available. To this aim, for the near future, we plan to extend the Penning gauge operation at AUG in order to allow measurements of Ne partial pressure, and potentially also Ar partial pressure, so to extend our experimental validation of SOLPS-ITER to Ne- and Ar-seeded plasmas. Helium pumping will also be studied in alternative divertor configurations at AUG [121] in the near future, after the installation of a new upper divertor with in-vessel coils [122]. Future dedicated SOLPS-ITER modelling will interpret the results and provide a comparison with what is observed in a conventional divertor. Future upper divertor studies at AUG will also benefit from the presence of a new cryopump coated with activated charcoal to trigger helium cryosorption [123]. This will be a unique possibility to study and develop power-exhaust-relevant scenarios in a device with efficient helium pumping, which is necessary to lay the foundations of operational scenarios for future devices. Additionally, we plan to extend our experimental on helium exhaust to ELM-free scenarios, so to assess the experimentally quantify the impact of ELM flushing on the measured He compression.

Acknowledgments

This work has been carried out within the framework of the EUROfusion Consortium, funded by the European Union via the Euratom Research and Training Programme (Grant Agreement No. 101052200–EUROfusion). Views and opinions expressed are however those of the author(s) only and do not necessarily reflect those of the European Union or the European Commission. Neither the European Union nor the European Commission can be held responsible for them.

Appendix A. Parallel force balance for He ions from SOLPS-ITER solutions

The parallel momentum balance equation applied on a He ion species in SOLPS-ITER, solved to self-consistently simulate the He ion velocity vector $\boldsymbol{v}_{\mathrm{He}}$ (and its parallel projection $v_{\parallel,\mathrm{He}} = \boldsymbol{v}_{\mathrm{He}} \cdot \boldsymbol{B}/B$), is based on the original Braginskii formulation, and reads [66, 77]

$$\begin{aligned}
&\left(\nabla \cdot \left(m_{\mathrm{He}} n_{\mathrm{He}} \boldsymbol{v}_{\mathrm{He}} \boldsymbol{v}_{\mathrm{He}}\right)\right)_{\parallel} \\
&\quad = -\nabla_{\parallel}\left(n_{\mathrm{He}} T_i\right) - e Z_{\mathrm{He}} n_{\mathrm{He}} \nabla_{\parallel} \Phi + m_e n_e n_{\mathrm{He}} \langle \sigma_{\mathrm{He}-e} \nu \rangle \\
&\qquad \times \left(v_{\parallel,e} - v_{\parallel,\mathrm{He}}\right) + \sum_{\beta} m_{\beta} n_{\beta} n_{\mathrm{He}} \langle \sigma_{\mathrm{He}-\beta} \nu \rangle \left(v_{\parallel,\beta} - v_{\parallel,\mathrm{He}}\right) \\
&\qquad + C_{\mathrm{He}-e} Z_{\mathrm{He}}^2 n_{\mathrm{He}} \nabla_{\parallel} T_e + \sum_{\beta} C_{\mathrm{He}-\beta} Z_{\mathrm{He}}^2 Z_{\beta}^2 \frac{n_{\mathrm{He}} n_{\beta}}{n_{\mathrm{He}} + n_{\beta}} \nabla_{\parallel} T_i \\
&\qquad + S_{\mathrm{mom,He}}.
\end{aligned} \tag{8}$$

Namely, the inertia of He ions (L.H.S. of equation (8)) is balanced by the sum of all forces present on the L.H.S., which are, in order of appearance:

- Static He ion pressure gradient.
- Electrostatic force.
- Electron friction force (with relative momentum transport rate coefficient $\langle \sigma_{\mathrm{He}-e} \nu \rangle$).
- Sum of the friction forces exerted by all other ion species β (with relative momentum transport rate coefficients $\langle \sigma_{\mathrm{He}-\beta} \nu \rangle$).
- Electron thermal force (with relative analytical coefficient $C_{\mathrm{He}-e}$).
- Sum of the thermal forces exerted by all other ion species β (with relative analytical coefficients $C_{\mathrm{He}-\beta}$).
- Volumetric momentum sources and sinks, i.e. due to transitions between neighboring ionized charge states and neutral source terms (from neutral-plasma collisions and recombinations).

In equation (8) the viscosity terms are neglected.

The achieved plasma solutions show that He ions have a near-zero inertia, and that electrostatic force and electron friction force are rather negligible with respect to the other forces. Additionally, the ion friction and thermal forces are dominated by the contribution of the main species, i.e. of the D^+ ions. As a result, one can write

$$\begin{aligned}
&-\nabla_{\parallel}\left(n_{\mathrm{He}} T_i\right) + m_{\mathrm{D}} n_{\mathrm{D}} n_{\mathrm{He}} \langle \sigma_{\mathrm{He}-\mathrm{D}} \nu \rangle \left(v_{\parallel,\mathrm{D}} - v_{\parallel,\mathrm{He}}\right) \\
&\quad + C_{\mathrm{He}-e} Z_{\mathrm{He}}^2 n_{\mathrm{He}} \nabla_{\parallel} T_e + C_{\mathrm{He}-\mathrm{D}} Z_{\mathrm{He}}^2 Z_{\mathrm{D}}^2 \frac{n_{\mathrm{He}} n_{\mathrm{D}}}{n_{\mathrm{He}} + n_{\mathrm{D}}} \nabla_{\parallel} T_i \approx 0.
\end{aligned} \tag{9}$$

Equation (9) will therefore determine the local value of the parallel velocity all the ionized He species, in terms of the parallel velocity of D^+ ions.

The improvements made to the default SOLPS-ITER physics model, described in the section 4.6, allowed to simulate different locations for the stagnation surface of He ions (cf figure 13). This comes from changes in the different terms in the balance (9), shown in figure 16 (referred to He^{2+} ions).

For all simulations, the sum of the shown forces is roughly zero, as predicted by equation (9).

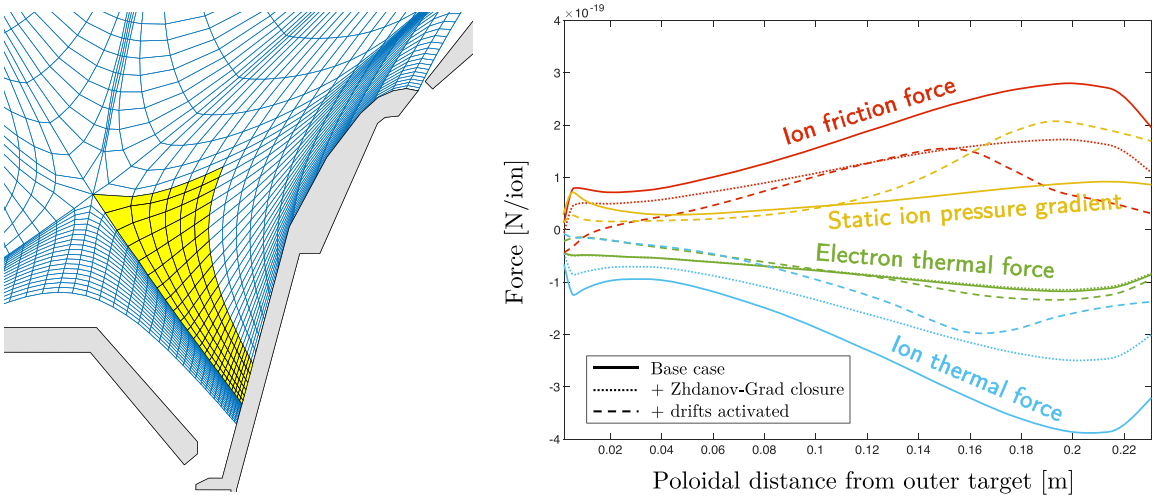

Figure 16. Changes in the parallel forces applied to the He^{2+} ions in the outer divertor region, radially averaged in the near SOL flux tubes, from target to X-point (i.e. corresponding to the yellow volume in the left plot): (i) in the base case (solid lines), (ii) when switching to the new Zhdanov-Grad closure scheme for the transport equations (dotted lines), and (iii) when also activating the drift terms (dashed lines).

When switching to the new Zhdanov-Grad scheme for the transport equations, ion friction force and ion thermal force applied on He^{2+} ions decrease in absolute values, while the other terms are roughly unchanged. The decrease of the ion friction force corresponds, therefore, to the local parallel velocity of He^{2+} ions becoming more similar to that of D^+ ions. The cause of this is smaller thermal force coefficients calculated using the Zhdanov-Grad module, with respect to the default SOLPS-ITER model [85], which cause a lower thermal force and, therefore, a lower friction force by balancing. This implies a shift of the stagnation surface of the He^{2+} ion flow towards that of the D^+ ion flow, i.e. towards upstream (cf figure 11), consistently with what shown in figure 13(*a*).

When also activating the drift terms, there is a further variation of all forces. This is caused by multiple characteristics of the divertor plasma solution changing after the activation of drifts, including electron density, electron temperature, parallel electron/ion temperature gradients and parallel flow velocities for the main species. Its interpretation is, therefore, not trivial. In any case, the net result is a further shift of the stagnation surface of the He ion flow towards upstream, as shown in the figure 13.

Appendix B. Conductance of a rarefied gas flow through a toroidally extended finite-length duct

The physical model used to emulate the resistance encountered by neutral gas flow while travelling from the subdivertor recycling volume to the pumping volume is an orifice with aperture length b, followed by a duct with length L. Since the surface which separates the two volumes extends in toroidal direction, the situation is the same as two reservoirs separated by an orifice and duct with rectangular cross sections in series, with long side $a = 2\pi R$ (where $R = 1.62$ m is the radius of the location of the duct) and short side b.

The conductance of this type of structures can be calculated analytically, assuming a free molecular flow [124, 125]. For a rectangular orifice with long side a and short side b, this is

$$\mathcal{L}_{\text{orifice}} = \frac{(a \cdot b) \cdot v_{\text{th}}}{4}, \tag{10}$$

while for a pipe with rectangular cross section, with long side a and short side b, and finite length L, this is

$$\mathcal{L}_{\text{pipe}} = \frac{4 \cdot (a \cdot b)^2 \cdot v_{\text{th}}}{3 \cdot 2 \cdot (a+b) \cdot L}. \tag{11}$$

Here, $v_{\text{th}} = \sqrt{\frac{8T}{\pi m}}$ is the thermal velocity of the gas, with temperature T and mass m. Since the combined effect of two conductances in series is given by $1/\mathcal{L}_{\text{tot}} = 1/\mathcal{L}_1 + 1/\mathcal{L}_2$, the total conductance is

$$\mathcal{L}_{\text{duct}} = \frac{1}{\frac{4}{(a \cdot b) \cdot v_{\text{th}}} + \frac{3 \cdot 2 \cdot (a+b) \cdot L}{4 \cdot (a \cdot b)^2 \cdot v_{\text{th}}}}. \tag{12}$$

Figure 17 shows the resulting conductance, calculated according to equation 12, as function of aperture b and duct length L, with a being the toroidal extension of the AUG vessel, and v_{th} calculated assuming a room temperature of $T = 300$ K for the gas and a mass $m = 4$ AMU for the gas particles. In our grid, we empirically regulated the dimensions of this duct in such a way to reproduce the experimentally observed pressure

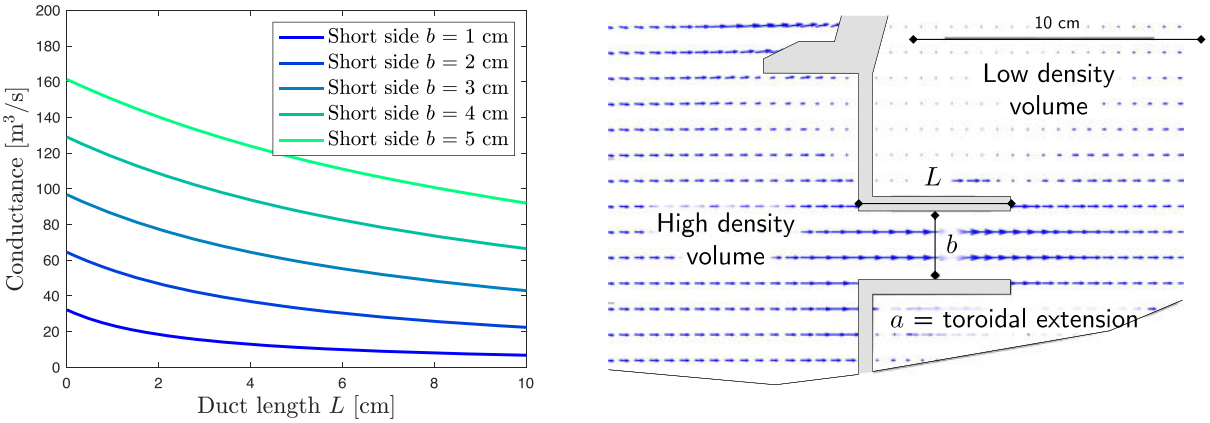

Figure 17. Left: analytical calculation of the conductance through the type of duct used to emulate the gas resistance effects in the simulations (equation (12)), as function of aperture b and duct length L, assuming a toroidal extension $a = 2\pi R$, with $R = 1.62$ m radius of the exact location of the duct, for a free molecular gas with temperature $T = 300$ K and mass $m = 4$ AMU. Right box: Geometry of the employed ducts, showing the one connecting recycling volume and pumping volume.

drop for the D_2 gas between recycling and pumping volumes, i.e. a subdivertor density ratio of roughly 4. To achieve this, we employed an aperture $b = 2.5$ cm and a pipe length $L = 5$ cm. According to equation (12), the theoretical conductance through this structure should be 45 m^{-3} s^{-1}.

ORCID iDs

A. Zito https://orcid.org/0000-0002-6743-6568
O. Pan https://orcid.org/0000-0003-3827-0674
A. Kappatou https://orcid.org/0000-0003-3341-1909
A. Kallenbach https://orcid.org/0000-0003-0538-2493
S.O. Makarov https://orcid.org/0000-0002-1799-7367
M. Cavedon https://orcid.org/0000-0002-0013-9753
U. Stroth https://orcid.org/0000-0003-1104-2233

References

[1] Reiter D. *et al* 1990 *Nucl. Fusion* **30** 2141
[2] Reiter D. *et al* 1991 *Plasma Phys. Control. Fusion* **33** 1579
[3] Pütterich T. *et al* 2019 *Nucl. Fusion* **59** 056013
[4] Loarte A. *et al* 2007 *Nucl. Fusion* **47** S203
[5] Kappatou A. *et al* 2019 *Nucl. Fusion* **59** 056014
[6] Stangeby P.C. 1990 *J. Nucl. Mater.* **176–177** 51–64
[7] Belo P. *et al* 2004 *Plasma Phys. Control. Fusion* **46** 1299
[8] Pütterich T. *et al* 2011 *J. Nucl. Mater.* **415** S334–9
[9] Neuhauser J. *et al* 1984 *Nucl. Fusion* **24** 39
[10] Neuhauser J. *et al* 1984 *J. Nucl. Mater.* **121** 194–8
[11] Stangeby P.C. and Elder J.D. 1995 *Nucl. Fusion* **35** 1391
[12] Shimizu K. *et al* 1997 *J. Nucl. Mater.* **241–243** 167–81
[13] Loarte A. 2001 *Plasma Phys. Control. Fusion* **43** R183
[14] Day C. *et al* 2014 *Fusion Eng. Des.* **89** 1505–9
[15] Groth M. *et al* 2001 *J. Nucl. Mater.* **290-293** 867–71
[16] Groth M. *et al* 2002 *Nucl. Fusion* **42** 591
[17] Zastrow K.-D. *et al* 2005 *Nucl. Fusion* **45** 163
[18] Bosch H.-S. *et al* 1997 *Plasma Phys. Control. Fusion* **39** 1771–92
[19] Bosch H.-S. *et al* 1999 *J. Nucl. Mater.* **266–269** 462–6
[20] Bosch H.-S. *et al* 2001 *J. Nucl. Mater.* **290–293** 836–9
[21] Sakasai A. *et al* 1999 *J. Nucl. Mater.* **266–269** 312–7
[22] Sakasai A. *et al* 2001 *J. Nucl. Mater.* **290–293** 957–61
[23] Wade M.R. *et al* 1995 *J. Nucl. Mater.* **220–222** 178–82
[24] Wade M.R. *et al* 1998 *Nucl. Fusion* **38** 1839
[25] Wiesen S. *et al* 2015 *J. Nucl. Mater.* **463** 480–4
[26] Bonnin X. *et al* 2016 *Plasma Fusion Res.* **11** 1403102
[27] Kukushkin A.S. *et al* 2009 *Nucl. Fusion* **49** 075008
[28] Kukushkin A.S. *et al* 2011 *Fusion Eng. Des.* **86** 2865–73
[29] Pacher H.D. *et al* 2011 *J. Nucl. Mater.* **415** S492–6
[30] Zito A. *et al* 2023 *Nucl. Fusion* **63** 096027
[31] Rohde V. *et al* 2009 *J. Nucl. Mater.* **390–391** 474–7
[32] Streibl B. *et al* 2001 *Fusion Eng. Des.* **56–57** 867–72
[33] McDermott R.M. *et al* 2018 *Plasma Phys. Control. Fusion* **60** 095007
[34] Summers H.P. and O'Mullane M.G. 2011 *AIP Conf. Proc.* **1344** 179–87
[35] Kappatou A. *et al* 2018 *Plasma Phys. Control. Fusion* **60** 055006
[36] Kremeyer T. *et al* 2020 *Rev. Sci. Instrum.* **91** 043504
[37] Haas G. and Bosch H.-S. 1998 *Vacuum* **51** 39–46
[38] Scarabosio A. *et al* 2009 *J. Nucl. Mater.* **390-391** 494–7
[39] Schneider R. *et al* 2006 *Contrib. Plasma Phys.* **46** 3–191
[40] Reiter D. *et al* 2005 *Fusion Sci. Technol.* **47** 172–86
[41] Kukushkin A.S. *et al* 2007 *J. Nucl. Mater.* **363–365** 308–13
[42] Eckstein W. 1994 *Radiat. Eff. Defects Solids* **130–131** 239–50
[43] Janev R. *et al* 1987 *Elementary Processes in Hydrogen-Helium Plasmas* (Springer)
[44] Kotov V. *et al* 2008 *Plasma Phys. Control. Fusion* **50** 105012
[45] Bachmann P. and Reiter D. 1995 *Contrib. Plasma Phys.* **35** 45–100
[46] Bhatnagar P.L., Gross E.P. and Krook M. 1954 *Phys. Rev.* **94** 511
[47] Reiter D. *et al* 1997 *J. Nucl. Mater.* **241-243** 342–8
[48] Kotov V. *et al* 2007 *Jülich-Rep.* 4257
[49] David P. *et al* 2021 *Nucl. Fusion* **61** 066025
[50] Manz P. *et al* 2020 *Phys. Plasmas* **27** 022506
[51] Zito A. *et al* 2021 *Plasma Phys. Control. Fusion* **63** 075003
[52] Fischer R. *et al* 2010 *Fusion Sci. Technol.* **58** 675–84
[53] Wolfrum E. *et al* 1993 *Rev. Sci. Instrum.* **64** 2285–92
[54] Willensdorfer M. *et al* 2014 *Plasma Phys. Control. Fusion* **56** 025008
[55] Murmann H. *et al* 1992 *Rev. Sci. Instrum.* **63** 4941–3
[56] Kurzan B. and Murmann H.D. 2011 *Rev. Sci. Instrum.* **82** 103501
[57] Viezzer E. *et al* 2012 *Rev. Sci. Instrum.* **83** 103501
[58] Cavedon M. *et al* 2017 *Rev. Sci. Instrum.* **88** 043103
[59] Reimold F. *et al* 2015 *J. Nucl. Mater.* **463** 128–34
[60] Chankin A.V. 1997 *J. Nucl. Mater.* **241–243** 199–213

[61] Rozhansky V. *et al* 2012 *Nucl. Fusion* **52** 103017
[62] Aho-Mantila L. *et al* 2017 *Plasma Phys. Control. Fusion* **59** 035003
[63] Kurzan B. *et al* 2021 *JINST* **16** C09012
[64] Reimold F. *et al* 2017 *Nucl. Mater. Energy* **12** 193–9
[65] Xiang L. *et al* 2017 *Nucl. Mater. Energy* **12** 1146–51
[66] Senichenkov I.Y. *et al* 2019 *Plasma. Phys. Control. Fusion* **61** 045013
[67] Hitzler F. *et al* 2020 *Plasma Phys. Control. Fusion* **62** 085013
[68] Senichenkov I.Y. *et al* 2023 *J. Nucl. Mater.* **34** 101361
[69] Rozhansky V. *et al* 2009 *Nucl. Fusion* **49** 025007
[70] Kallenbach A. *et al* 2024 *Nucl. Fusion* **64** 056003
[71] Goto M. 2003 *J. Quant. Spectrosc. Radiat. Transfer* **76** 331–44
[72] Linehan B.L. *et al* 2023 *Nucl. Fusion* **63** 036021
[73] Cavedon M. *et al* 2017 *Plasma Phys. Control. Fusion* **59** 105007
[74] Kukushkin A.S. *et al* 2005 *Nucl. Fusion* **45** 608
[75] Kukushkin A.S. *et al* 2007 *Nucl. Fusion* **47** 698
[76] Kukushkin A.S. and Pacher H.D. 2016 *Nucl. Fusion* **56** 126012
[77] Rozhansky V. *et al* 2015 *J. Nucl. Mater.* **463** 477–9
[78] Henderson S.S. *et al* 2023 *Nucl. Fusion* **63** 086024
[79] Coster D.P. *et al* 1997 *J. Nucl. Mater.* **241–243** 690–5
[80] Schneider R. *et al* 1997 *J. Nucl. Mater.* **241–243** 701–6
[81] Schneider R. *et al* 1999 *J. Nucl. Mater.* **266–269** 175–81
[82] Neu R. *et al* 2003 *Nucl. Fusion* **43** 1191
[83] Sytova E. *et al* 2018 *Contrib. Plasma Phys.* **58** 622–8
[84] Sytova E. *et al* 2020 *Phys. Plasmas* **27** 082507
[85] Makarov S.O. *et al* 2021 *Phys. Plasmas* **28** 062308
[86] Makarov S.O. *et al* 2022 *Contrib. Plasma Phys.* **62** e202100165
[87] Sharipov F. *et al* 2009 *J. Vacuum Sci. Technol.* A **27** 479–84
[88] Varoutis S. *et al* 2012 *Vacuum* **86** 1952–9
[89] Varoutis S. *et al* 2017 *Fusion Eng. Des.* **121** 13–21
[90] Coster D.P. *et al* 2001 *J. Nucl. Mater.* **290–293** 845–8
[91] Roth J. *et al* 1992 *Nucl. Fusion* **32** 1835
[92] Angioni C. *et al* 2009 *Nucl. Fusion* **49** 055013
[93] Angioni C. 2021 *Plasma Phys. Control. Fusion* **63** 073001
[94] Wischmeier M. 2015 *J. Nucl. Mater.* **463** 22–29
[95] Loarte A. *et al* 2017 *Fusion Eng. Des.* **122** 256–73
[96] Pacher H.D. *et al* 2007 *J. Nucl. Mater.* **363–365** 400–6
[97] Zohm H. *et al* 2013 *Nucl. Fusion* **53** 073019
[98] Sedgley D.W. 1989 *Fusion Eng. Des.* **10** 217–22
[99] Kim J. *et al* 1990 *J. Vacuum Sci. Technol.* A **8** 3084–7
[100] Day C. *et al* 2008 *Vacuum* **83** 773–8
[101] Pearce R.J.H. *et al* 2013 *Fusion Eng. Des.* **88** 809–13
[102] Day C. *et al* 2022 *Fusion Eng. Des.* **179** 113139
[103] Pacher H.D. *et al* 2009 *J. Nucl. Mater.* **390–391** 259–62
[104] Pacher H.D. *et al* 2015 *J. Nucl. Mater.* **463** 591–5
[105] Dux R. *et al* 2011 *Nucl. Fusion* **51** 053002
[106] Laggner F.M. *et al* 2018 *Plasma Phys. Control. Fusion* **60** 025002
[107] Viezzer E. *et al* 2020 *Plasma. Phys. Control. Fusion* **62** 024009
[108] Fundamenski W. *et al* 2006 *Plasma Phys. Control. Fusion* **48** 109–56
[109] Moulton D. *et al* 2013 *Plasma Phys. Control. Fusion* **55** 085003
[110] van Vugt D.C. *et al* 2019 *Phys. Plasmas* **26** 042508
[111] Coster D.P. *et al* 2015 *J. Nucl. Mater.* **463** 620–3
[112] Tskhakaya D. *et al* 2008 *Contrib. Plasma Phys.* **48** 89–93
[113] Stegmeir A. *et al* 2019 *Phys. Plasmas* **26** 052517
[114] Zholobenko W. *et al* 2021 *Plasma. Phys. Control. Fusion* **63** 034001
[115] Hoelzl M. *et al* 2021 *Nucl. Fusion* **61** 065001
[116] Korving S.Q. *et al* 2023 *Phys. Plasmas* **30** 042509
[117] Cathey A. *et al* 2020 *Nucl. Fusion* **60** 124007
[118] Senichenkov I.Y. *et al* 2023 Comparison of different seeding impurities (N, Ne, Ar, Kr) compression effectiveness in divertor by SOLPS-ITER modeling *29th IAEA Fusion Energy Conf.* (*London*) p CN-316-1630
[119] Pitts R.A. *et al* 2011 *J. Nucl. Mater.* **415** S957–64
[120] Pitts R.A. *et al* 2019 *Nucl. Mater. Energy* **20** 100696
[121] Pan O. *et al* 2020 *Plasma Phys. Control. Fusion* **62** 045005
[122] Lunt T. *et al* 2017 *Nucl. Mater. Energy* **12** 1037–42
[123] Schall G. *et al* 2021 *Fusion Eng. Des.* **166** 112316
[124] Knudsen M. 1909 *Ann. Phys., NY* **28** 75
[125] Smoluchowski M. 1910 *Ann. Phys., NY* **33** 1559